



## NO<sub>x</sub> reduction in the Di-Air system over noble metal promoted ceria

Yixiao Wang, Freek Kapteijn, Michiel Makkee\*

Catalysis Engineering, Chemical Engineering Department, Delft University of Technology, Van der Maasweg 9, 2629 HZ Delft, The Netherlands



### ARTICLE INFO

**Keywords:**  
Selective NO reduction  
Ceria  
Noble metal  
Raman  
TAP  
FT-IR

### ABSTRACT

In this study, the role of the noble metals Pt and Rh (0.5 wt.%) for the selective reduction of NO into N<sub>2</sub> is evaluated by the transient TAP technique and in-situ spectroscopy using a commercial stable ceria support (denoted as CZ) and applying isotopically labelled <sup>15</sup>NO and <sup>18</sup>O<sub>2</sub>. The transient operation was mimicked by multi-pulse oxidation (using O<sub>2</sub> or NO) and reduction cycles (using CO, H<sub>2</sub>, C<sub>3</sub>H<sub>6</sub> and C<sub>3</sub>H<sub>8</sub>), while following quantitatively the catalyst and reactants response. Pt and Rh significantly lowered the temperature of CZ reduction. CO and H<sub>2</sub> only reduce the surface of CZ, while a 2.5 times deeper reduction was achieved by the hydrocarbons C<sub>3</sub>H<sub>6</sub> and C<sub>3</sub>H<sub>8</sub>, removing also lattice oxygen. Pt and Rh also promoted carbon deposition after surface reduction. Rh was a more active promoter than Pt, while propene was more reactive than propane over both metals. During the NO reduction the pre-reduced CZ support became gradually re-oxidised and after filling 70–80% of the oxygen vacancies the NO started to appear in the product mixture. In the presence of carbon deposits the lattice oxygen of the CZ reacted with the carbon keeping the CZ in a reduced state, extending the NO decomposition process as long as the carbon was present. The reduction of NO over pre-reduced noble metal/CZ showed a selective formation N<sub>2</sub>, while N<sub>2</sub>O and NO<sub>2</sub> were never observed. During the NO reduction process some unidentified N-species remained on the catalyst, the amount depending on the type of catalyst, but finally all nitrogen was released as N<sub>2</sub>. The presence of the noble metal led less unidentified N-species on the CZ surface and to a faster N<sub>2</sub> formation rate than that over the bare CZ.

### 1. Introduction

Nitrogen oxides (NO<sub>x</sub>) are harmful gasses, causing every year millions of premature deaths of people [1,2]. Around 40% of the total NO<sub>x</sub> released into the atmosphere originated from road transport [1,3]. The actual average NO<sub>x</sub> emission from cars on the road is six to eight times higher than the actual emission limit [4]. Therefore, as of September 2017, the European Commission will proclaim that the real driving emission (RDE) test will partially replace the current laboratory test upon the introduction of new car models into the market [5]. However, up to 2.1 times higher NO<sub>x</sub> emission (0.168 g/km), relatively to the current Euro 6 NO<sub>x</sub> emission standard (0.08 g/km), is allowed under this RDE test by September 2017 [5]. The fact that a higher NO<sub>x</sub> emission by the new legislation in 2017 is allowed indicates that currently available technologies: Urea- Selective Catalytic Reduction (SCR) [6–8], NO<sub>x</sub> Storage and Reduction (NSR) [9–11], and combinations thereof still need to be significantly improved. In future, it can be anticipated that the NO<sub>x</sub> emission limit will become even more stringent. Therefore, more efficient or alternative, more advanced exhaust emissions after-treatment technologies for lean-burn engines will be required. The Di-Air system [12], under development by Toyota Motor

Company, shows promise to meet the future NO<sub>x</sub> emission standards under real driving test conditions. The Di-Air system retains high NO<sub>x</sub> conversion levels (above 80%) even up to 800 °C and high gas hourly space velocities (GHSV) up to 120.000 L/L/h, where other systems are less active. Short fuel rich and lean periods are created by direct injection of hydrocarbons (HC's) at a high frequency downstream of the engine in the exhaust system upstream of a complex NSR catalyst (Pt/Rh/Ba/K/Ce/Al<sub>2</sub>O<sub>3</sub>) [12]. Investigation on the role of each catalyst component is essential for understanding how the system works and its further improvement.

Ceria is an essential catalyst ingredient in the Di-Air system due to its redox properties, since it can act as an oxygen buffer [13]. Under rich (fuel injection) conditions its lattice oxygen can react with hydrocarbons, CO, and H<sub>2</sub> [14,15]. HC's injection is essential to create a deep reduction degree of ceria and deposition of carbon onto ceria [12,16]. The created oxygen vacancies (reduced ceria) were found to selectively convert NO into (di)nitrogen (N<sub>2</sub>) [13], even in the presence of an excess of oxygen [17] and CO<sub>2</sub> [18]. The deposited carbon was oxidised by oxygen species from the lattice oxygen of ceria under oxidative conditions, recreating new oxygen anion vacancies, thereby increasing substantially the NO reduction capacity.

\* Corresponding author.

E-mail address: [m.makkee@tudelft.nl](mailto:m.makkee@tudelft.nl) (M. Makkee).

The temperature required for the reduction of the commercially bare Ceria composite by hydrocarbons (HCs), however, needed to exceed 500 °C for C<sub>3</sub>H<sub>6</sub> and 540 °C for C<sub>3</sub>H<sub>8</sub> used as reductant. The reactivity of oxygen in the ceria lattice is too low to activate the C<sub>3</sub>H<sub>6</sub> and C<sub>3</sub>H<sub>8</sub> at temperatures below 500 °C [15]. Considering automotive conditions, especially during the cold start, the reduction of ceria may be difficult. For practical application of ceria-based catalysts it may be beneficial to add promoters, e.g. noble metals that could assist ceria reduction at lower temperatures. After hydrocarbon treatment of ceria at 300 °C Yao and Yao [14] found no oxygen storage capacity (OSC) and a limited capacity at 400 °C, meaning that HCs cannot reduce surface oxygen of ceria at temperatures below 300–350 °C. After addition of Pt, Pd, or Rh to ceria, however, a substantial OSC even at 300 °C was evidenced. Much research have been performed on <sup>18</sup>O/<sup>16</sup>O isotope exchange, a common method used to study the adsorption/desorption properties of oxygen and the participation of lattice oxygen from ceria in oxidation reactions, by using either <sup>18</sup>O<sub>2</sub> or C<sup>18</sup>O<sub>2</sub> over the ceria and noble metal loaded ceria [19,20]. The presence of noble metals was found to accelerate the exchange rate of oxygen from either <sup>18</sup>O<sub>2</sub> or C<sup>18</sup>O<sub>2</sub> in the lower temperature range as compared to bare ceria. Although improved oxygen exchange phenomena are no direct evidence for affecting reduction, it is an indication that the presence of noble metals may affect the reactivity of oxygen from the ceria lattice with HCs or carbonaceous deposits in the absence of gas-phase O<sub>2</sub>.

The aim of this study is to investigate the role of the noble metals Pt and Rh on ceria for its reduction by HCs and performance in subsequent NO reduction. For this purpose, C<sub>3</sub>H<sub>6</sub> and C<sub>3</sub>H<sub>8</sub> were used as a fuel model reductant. Temporal Analysis of Products (TAP) was mainly used for the quantification of the degree of reduction of the ceria support and the NO reduction mechanism. Additionally, in-situ Raman spectroscopy performed in a fixed bed reactor was applied to support the TAP results.

A commercial Zr- and La-doped ceria is used as a model ceria system mainly for its high hydrothermal stability and enhanced oxygen lattice diffusion [13,21,22].

## 2. Experimental

### 2.1. Materials preparation

Pt/CZ and Rh/CZ, aimed at 0.5 wt.% noble metal loading were prepared via an incipient wetness impregnation method on vacuum dried Zr-La doped ceria (a gift of Engelhard, now BASF, further denoted as CZ). The bulk atomic ratio of Ce, La and Zr is 0.64:0.15:0.21. Tetra-ammine platinum (II) nitrate and rhodium(III) nitrate hydrate purchased from Sigma-Aldrich, were used as precursors, dissolved in purified demi water. Subsequently, the samples (thin layer in a crucible) were dried at 110 °C overnight and calcined at 550 °C for 5 h in a static air furnace.

### 2.2. Characterisation

#### 2.2.1. N<sub>2</sub> adsorption

N<sub>2</sub> adsorption at –196 °C (Tristar II 3020) Micromeritics was used to determine the textural properties like BET area and pore volume. The catalyst samples were pre-treated by degassing at 200 °C for 16 h in vacuum (0.05 mbar).

#### 2.2.2. Inductively coupled plasma optical emission spectroscopy (ICP-OES)

Approximately 50 mg of samples were digested in 4.5 mL 30% HCl + 1.5 mL 65% HNO<sub>3</sub> using microwave irradiation for 120 min with a power of 900 W. After the destruction, the samples were diluted to 50 mL with Millipore-Q (purified demi) water. The samples were analysed with ICP-OES (PerkinElmer Optima 5300).

#### 2.2.3. X-Ray photoelectron spectroscopy (XPS)

XPS measurements were recorded on a K-alpha Thermo Fisher

Scientific spectrometer using mono-chromated Al K $\alpha$  radiation. A flood gun was applied for charge compensation. Fixed Lorentz function was used to analyse the peak intensities. Binding energies were calibrated with C(1s) at 285 eV as reference.

#### 2.2.4. X-ray diffraction (XRD)

The powder X-Ray diffraction (XRD) was recorded by a Bruker-AXS D5005 with a Co K $\alpha$  source. The data was collected three times by varying the 2θ angle from 5° to 90° with a step size of 0.02.

#### 2.2.5. Transmission electron microscope (TEM)

Transmission Electron Microscopy (TEM) images were recorded on a JEM-2100P electron microscope operating at 200 kV. Prior to transfer the samples into the TEM analysis chamber, the samples were dispersed in ethanol and deposited onto a carbon-coated copper grid, shortly dried in air and, subsequently, inserted into the vacuum system of the microscope.

#### 2.2.6. Raman microscopy

Raman spectra of samples were collected by a Renishaw in Via Reflex confocal Spectrometer. The excitation wavelength was 325 nm. The power of each laser line was kept at about 2.5 mW to prevent local heating. The resolution of the spectrometer was 1 cm<sup>–1</sup>.

#### 2.2.7. Temperature programmed reaction (TPR)

TPR (H<sub>2</sub>) of all the samples were carried out in a fixed bed reactor system connected to a thermal conductivity detector (TCD) to monitor the consumption of hydrogen by the catalyst. Catalyst samples (200 mg) were packed between SiC layers (300–425 μm). The sample was then reduced in a 10% H<sub>2</sub>/Ar flow of 30 mL<sub>STP</sub>/min by increasing temperature from room temperature to 1000 °C with a heating rate of 5 °C/min. TCD was calibrated by using CuO as a reference. A permapure tubular drier was used to remove the water produced during the reduction step upstream of the TCD detector.

### 2.3. TAP pulse experiments between 450 °C and 500 °C

The pulse experiments were performed in an in-house developed and constructed TAP (Temporal Analysis of Products) reactor. Series of small gas pulses, typically in the order of 1.10<sup>15</sup> molecules, were introduced in a small volume upstream of the catalyst packed bed reactor. The produced pressure gradient over the catalyst packed bed thereby causes the molecules to be transported through the packed bed to the ultra-low vacuum at the opposite side of the packed bed. Depending on the actual number of molecules pulsed, the transport will be in the pure Knudsen diffusion regime. In other words, the molecules interact only with the “walls” (catalyst surface and reactor walls) of the system and not with each other. Upon interaction with the catalyst, molecules can be converted into different products. The evolution of the reactant and product molecules is tracked (one mass *m/e* unit per pulse) with a high time resolution of 10 kHz using a quadrupole mass spectrometer. A careful calibration of the MS ensured a quantitative analysis, and overall mass balances could be closed within 5–15% accuracy. Details about TAP can be found elsewhere [13].

#### 2.3.1. Multi-pulse TAP experiment

10 mg Rh/CZ and Pt/CZ were used in the TAP reactor at 450 °C. In all experiments a starting pulse size of approximately 2·10<sup>15</sup> molecules was used (including reactants and inert gas used as internal standard), the pulse size gradually decreases during an experiment as the reactant was pulsed from a closed and calibrated volume of the pulse-valve line. Prior to a reduction, the catalyst was firstly (re-)oxidised at the same temperature at which the reduction was performed, using pulses of 80 vol. % O<sub>2</sub> in Ar until a stable O<sub>2</sub>/Ar signal ratio downstream of the reactor was obtained. The reduction was carried out by injecting reductant pulses of either 80 vol. % C<sub>3</sub>H<sub>6</sub> in Ne, 80 vol. % C<sub>3</sub>H<sub>8</sub> in Ne,

80 vol. % CO in Ar, or 66.7 vol. % H<sub>2</sub> in Ar until a stable reactant and product to an internal standard signal ratio was obtained, indicating that the catalyst was “equilibrated”. <sup>15</sup>NO and <sup>18</sup>O<sub>2</sub> pulse experiments were performed using 80 vol. % <sup>15</sup>NO in Kr, and 5 vol. % <sup>18</sup>O<sub>2</sub> in He, respectively.

The pulse size of reactant at each pulse number was determined by fitting the pulse valve pressure using the exponential equation:

$$P(n) = Ae^{Bn} \text{ (nisthepulsenumber)}$$

All relevant MS signal were calibrated and quantified at room temperature by using 200 mg quartz beads (particle size 150–212 μm) fully filled stainless steel SS3 316 reactor. Detailed TAP quantification method can be found elsewhere [13].

The consumption of the oxygen species from the catalyst and the carbon species deposited during C<sub>3</sub>H<sub>8</sub> and C<sub>3</sub>H<sub>6</sub> multi-pulse experiments were calculated using the following atomic balances:

$$n_{O,\text{consumed}} = n_{H_2O,\text{obs}} + n_{CO,\text{obs}} + 2n_{CO_2,\text{obs}} \quad (1)$$

$$n_{C,\text{deposited}} = 3n_{C_3H_6,\text{in}}(C_3H_8,\text{in}) - 3n_{C_3H_6,\text{obs}}(C_3H_6,\text{obs}) - n_{CO,\text{obs}} - n_{CO_2,\text{obs}} \quad (2)$$

where *n* is the number of molecules or atoms of the specified species observed (obs), consumed or introduced (in) over the whole series of pulses.

The number of oxygens consumed during the C<sub>3</sub>H<sub>8</sub> and C<sub>3</sub>H<sub>6</sub> multi-pulse experiments are equal to the number of oxygen vacancies created in the ceria lattice.

Similarly, the amount of oxygen accumulation and carbon consumption during the <sup>15</sup>NO multi-pulse experiments were calculated using the following atomic balance:

$$n_{O,\text{accumulated}} = n_{NO,\text{in}} - n_{CO,\text{obs}} - 2n_{CO_2,\text{obs}} - n_{N_2O,\text{obs}} - 2n_{NO_2,\text{obs}} - n_{NO,\text{obs}} \quad (3)$$

$$n_{C,\text{consumed}} = -n_{CO,\text{obs}} - n_{CO_2,\text{obs}} \quad (4)$$

$$n_{N,\text{accumulated}} = n_{NO,\text{in}} - n_{NO,\text{obs}} - 2n_{N_2O,\text{obs}} - 2n_{N_2O,\text{obs}} - n_{NO_2,\text{obs}} \quad (5)$$

### 2.3.2. Pump-probe TAP experiments

Pump-probe TAP experiments were performed using two pulse valves to consecutively inject <sup>15</sup>NO and <sup>14</sup>NO, respectively. Rh/CZ and CZ were used at 450 and 500 °C, respectively. Before the pump-probe experiment, multi-pulse experiments were conducted to reduce the catalysts by H<sub>2</sub>, then <sup>15</sup>NO/Kr and <sup>14</sup>NO/Ar mixtures were subsequently injected in an alternating sequence, and the *m/e* intensity of <sup>15</sup>N<sub>2</sub>, <sup>15</sup>N<sup>14</sup>N, <sup>14</sup>N<sub>2</sub>, <sup>14</sup>NO, and <sup>15</sup>NO were measured during each pulse for a time interval of 5 s. The injection time was *t* = 0 for <sup>15</sup>NO/Kr and *t* = 5 s later for <sup>14</sup>NO/Ar.

### 2.3.3. Single pulse TAP experiments

Single pulse TAP experiments were performed to investigate the

interaction of N<sub>2</sub> with a pre-oxidised or pre-reduced catalyst bed using one single pulse of N<sub>2</sub> at 450 °C. To reduce the catalyst, 10000 pulses of H<sub>2</sub> were required.

### 2.4. In-situ Raman spectroscopy

The Raman spectroscopy measurements were performed under reaction conditions by using an AvaRaman-PRB-FC Raman probe. The catalyst sample (200 mg) was placed a 6 mm inner diameter quartz reactor tube and downstream equipped with a mass spectrometer (MS, Hiden Analytical, HPR-20 QIC) and infrared (IR) spectroscopy (Perkin-Elmer, Spectrum One), both for gas-phase analysis. For the IR analysis a gas cell with KBr windows with a path length of ~5 cm was used. The spectra were recorded in a continuous mode using the Perkin-Elmer “Time-Base” software between 4000–700 cm<sup>-1</sup> wavenumbers with a spectral resolution of 8 cm<sup>-1</sup> and an acquisition of 8 scans per spectrum, resulting in a time interval of 23 s between each displayed spectrum. Raman data were collected using a Kaiser Optical Systems RXN spectrometer with a diode laser operating at 532 nm and output power of 10 mW. AvaRaman-PRB-FC Raman probe was used to focus the laser beam to a spot and to collect the scattered radiation behaviour. A CCD camera was used to record the data using the Thermo Galactic Grams AI v. 7.0 software. Spectra were acquired using 2 scans at a resolution of 0.3 cm<sup>-1</sup> in the range between 100 (detector cutoff) and 4350 cm<sup>-1</sup>.

A feed composition of 0.2% NO (He balance) was used with a GHSV of 67.000 L/L/h. Prior to feeding NO, the catalyst was pre-treated by 1.25% C<sub>3</sub>H<sub>6</sub> in He for 2 h and flushed with He (200 mL/min) for 30 min afterwards, both at 500 °C.

## 3. Results

### 3.1. Characterisation

#### 3.1.1. Structure and chemical composition

Characterisation details of the CZ support were reported elsewhere [13,23]. In brief, the typical fluorite structure of ceria was confirmed by Raman and XRD. The BET area was 65 ± 2 m<sup>2</sup>/g. The crystal size of CZ determined by the Scherrer's equation and TEM measurements were on average 5.0 ± 0.6 nm.

The BET areas of Pt/CZ and Rh/CZ were similar to that of the support (65 ± 2 m<sup>2</sup>/g). Measured by ICP-OES, the mass loadings of Pt and Rh were determined to be the targeted 0.5 wt %. Fig. 1A shows the XPS spectrum of Pt(4f). 4f<sub>7/2,5/2</sub> peaks of PtO were observed at 71.5 and 74.9 eV with the spin-orbit splitting around 3.5 eV. 4f<sub>7/2,5/2</sub> peaks of PtO<sub>2</sub> were found at 74 and 77.2 eV (Fig. 1A). Survey XPS spectra are shown in Figs. S1, SI. These binding energies for Pt are in good accordance with the literature values [24]. Fig. 1B shows the XPS

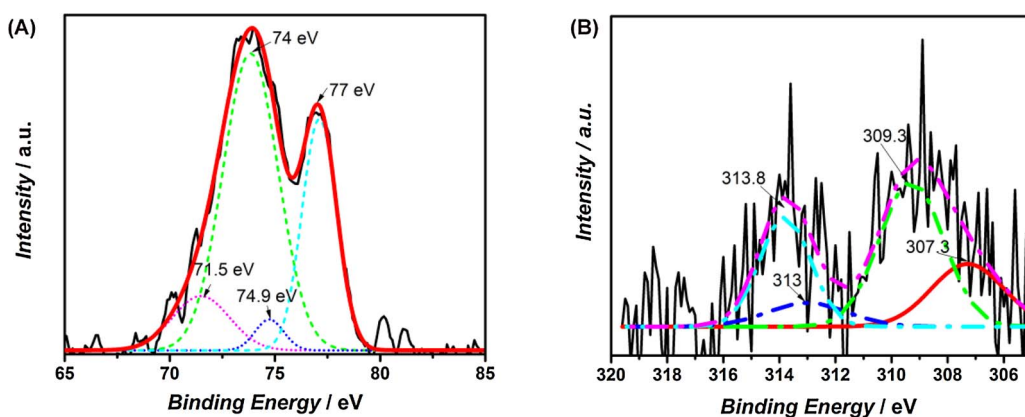


Fig. 1. XPS of Pt(4f) and Rh(3d) core level region of (A) Pt/CZ and (B) Rh/CZ, respectively.

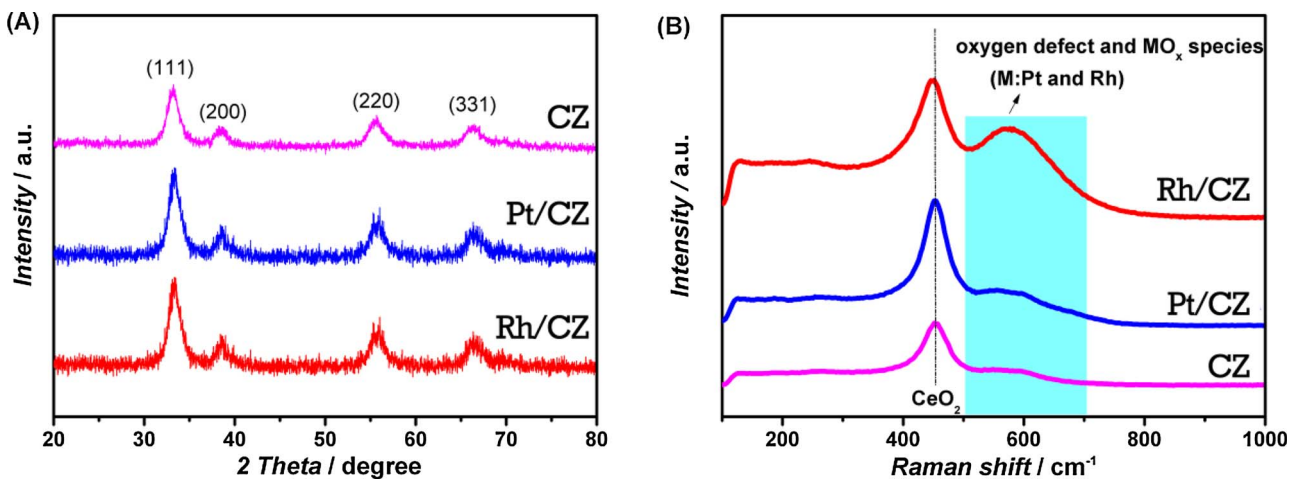


Fig. 2. XRD patterns (A) and Raman spectra (B) of oxidised Pt/CZ, Rh/CZ, and CZ.

spectrum of Rh/CZ, corresponding to the electronic transitions Rh  $3d_{3/2}$  and Rh  $3d_{5/2}$ , with binding energies at 313 eV and 306–310 eV [25], respectively. 307 eV and 309 eV were assigned to the presence of Rh<sup>+</sup> and Rh<sup>3+</sup> of Rh  $3d_{5/2}$ , respectively [25,26].

Fig. 2A shows the XRD patterns of Pt/CZ, Rh/CZ, and the CZ support. The patterns of noble metal loaded samples showed the fluorite cubic structure of CeO<sub>2</sub>. Diffraction lines due to Rh and Pt metals or to any platinum oxides or rhodium oxides were not observed (below the detection of the XRD apparatus due to the low noble metal loading and high dispersion). The presence of a peak at around 460 cm<sup>-1</sup> in the Raman spectra (Fig. 2B) was due to the characteristic ceria fluorite peak, assigned to the  $F_{2g}$  mode. This peak presented a shoulder between 500 and 700 cm<sup>-1</sup> including contributions of vacant sites of the CZ support and MO<sub>x</sub> (PtO<sub>x</sub> or RhO<sub>x</sub>) species [25,27,28].

Fig. 3 shows the TEM micrographs of Pt/CZ and Rh/CZ (TEM (Fig. 3A and C) micrographs and STEM (Fig. 3B and D) micrographs). Pt and Rh nanoparticles were circled in red in Fig. 3A and C, respectively. The red arrows pointed the presence of Pt and Rh on CZ support in Fig. 3B and D, respectively. However, the molar masses of the noble metals and cerium, however, were very close yielding a low contrast in the STEM micrograph (Fig. 3B and D). In combination with the low mass loadings of Pt and Rh (0.5 wt.%), the noble metal particle size distributions could not be adequately determined. The interplanar spacing of 0.32 nm in inset of Fig. 3C and D corresponded to the (111) plane of ceria support [29]. Lattice fringes of 0.23 nm (inset of Fig. 3A) and 0.26 nm (inset of Fig. 3C) can be ascribed to (1 1 1) planes of Pt [30] and Rh<sub>2</sub>Ce(220) [31].

### 3.1.2. TPR ( $H_2$ )

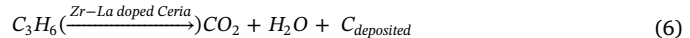
The reduction properties of Pt/CZ, Rh/CZ, and CZ were conducted by TPR ( $H_2$ ), and the results are presented in Fig. 4. ceria showed two peaks centred at 430 and 550 °C. The low temperature (430 °C) process was attributed to the surface reduction and the high temperature (550 °C) accounted for the bulk reduction [14]. As compared to the ceria support, the surface and bulk reduction of noble metal loaded ceria significantly shifted to a lower temperature. The maximum reduction peak temperatures are given in Table 1. As shown in Table 1, the total  $H_2$  consumption for ceria support, Pt/CZ, and Rh/CZ are 0.31, 0.36, and 0.43 mol  $H_2$ /mol Ce.

## 3.2. Multi-pulse TAP experiments

### 3.2.1. Reduction of noble metal loaded CZ

The reduction of noble metal loaded CZ catalysts was investigated by using CO,  $H_2$ ,  $C_3H_6$ , and  $C_3H_8$  as reductant in TAP. As an example for a noble metal, Fig. 5A and B shows the result of  $C_3H_6$  (propene) pulses

over the pre-oxidised Pt/CZ at 450 °C. Two types of  $C_3H_6$  reactions were observed:  $C_3H_6$  oxidation to  $CO_2$  and  $H_2O$  and  $C_3H_6$  oxidative cracking/dehydrogenation, as described by Eqs. (6) and (7), respectively.  $C_3H_6$  experienced a full conversion till pulse number 500.



During the complete  $C_3H_6$  oxidation period (pulse number 0–50), the main oxidation products were  $CO_2$  and  $H_2O$  and only a small amount of  $CO$  was observed. The  $H_2$  formation considerably increased after pulse number 50, accompanied by a significant decline of the  $H_2O$  formation.  $CO$  formation increased after pulse number 90, where  $CO_2$  formation significantly dropped with pulse number. During the pulse number from 50 to 1000 oxidative hydrocarbon cracking was the main reaction with the formation of  $CO$  and  $H_2$ . The oxygen and carbon balances at each  $C_3H_6$  pulse are displayed in Fig. 5B. The formation of  $CO_2$ ,  $H_2O$ , and  $CO$  caused partial reduction of CZ from  $Ce^{4+}$  to  $Ce^{3+}$ . Carbon deposition was calculated during both the complete oxidation and cracking reactions. The pulses of (propane)  $C_3H_8$  over Pt/CZ showed a similar product evolution as that for the (propene)  $C_3H_6$  pulses, although the  $C_3H_8$  showed full conversion till pulse number 150 (Figs. S2, SI). Rh/ceria showed the same trends as Pt/CZ during the both  $C_3H_6$  and  $C_3H_8$  pulses at 450 °C (Fig. 5C and D and S3, SI), but the carbon deposits for the Rh/CZ were significantly higher than those on Pt/CZ upon  $C_3H_6$  multi-pulse exposure (Table 2).

Additionally, pulsing  $CO$  over both noble metal loaded CZ led to  $CO_2$  formation. Hardly any carbon was deposited on the catalyst over during the  $CO$  pulses (Figs. S4 and S5, SI).  $H_2$  pulsing over the noble metal loaded CZ resulted in the quantitative formation of  $H_2O$  (Figs. S6 and S7, SI). The total number of oxygen extracted during  $CO$  and  $H_2$  exposures are given in Table 2.

### 3.2.2. NO reduction

3.2.2.1.  $^{15}NO$  Pulses after  $H_2$  reduction. The reduction of NO over  $H_2$  reduced noble metals loaded CZ support was investigated in TAP by using  $^{15}NO$ . Fig. 6 shows the products and reactant evolution during the  $^{15}NO$  pulses over  $H_2$  reduced Pt/CZ and Rh/CZ at 450 °C. For the Pt/CZ (Fig. 6A), the full  $^{15}NO$  conversion was observed with  $^{15}N_2$  as the exclusive product from pulse number 0 to 700. Moreover, around 70% of oxygen vacancies were refilled by  $^{15}NO$  before the breakthrough of  $^{15}NO$ . There was no  $N_2O$  and  $NO_2$  formation in that time frame. Similarly to Pt/CZ, Rh showed full  $^{15}NO$  conversion till pulse number 900, where 80% of oxygen vacancies were refilled by  $^{15}NO$  (Fig. 6B).  $^{15}N_2$  was the exclusive product and no  $N_2O$  and  $NO_2$  formation were observed. It should be noted that some nitrogen species temporarily

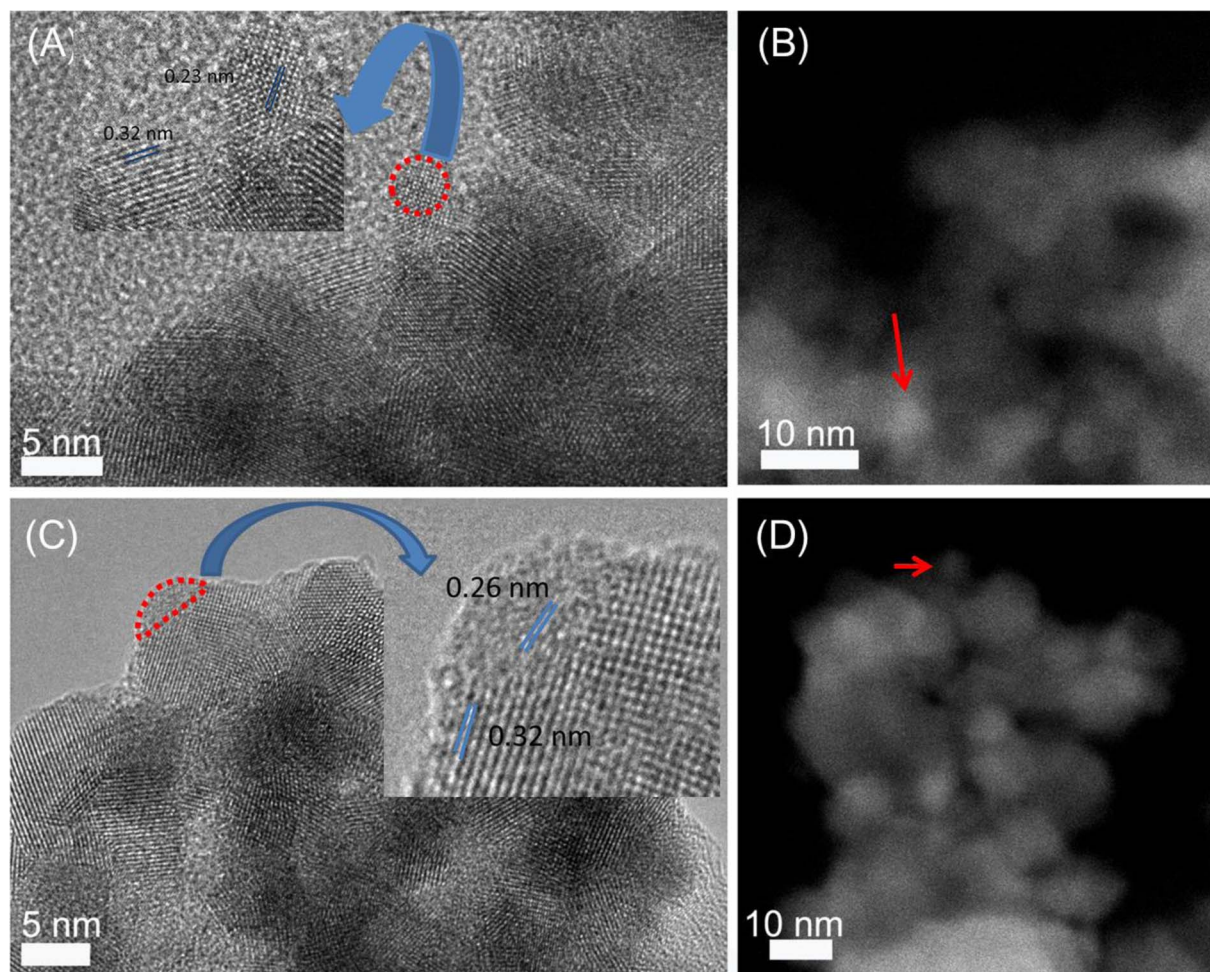


Fig. 3. HR-TEM and STEM micrographs of oxidised Pt/CZ (A and B) and Rh/CZ (C and D). Red circles and arrows point to a metal particle. (For interpretation of the references to colour in this figure legend, the reader is referred to the web version of this article).

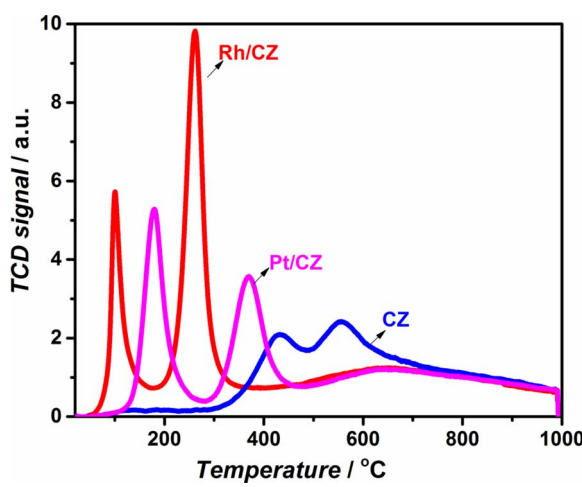


Fig. 4. TPR ( $\text{H}_2$ ) profiles of CZ, Pt/CZ, and Rh/CZ.

accumulated on the samples.

**3.2.2.2.  $^{15}\text{NO}$  Pulses after hydrocarbon reduction.** The NO reduction into nitrogen over the hydrocarbons reduced noble metals loaded CZ support was investigated in TAP by using  $^{15}\text{NO}$  to distinguish its products from CO and  $\text{N}_2$  ( $m/e = 28$ ) and  $\text{CO}_2$  from  $\text{N}_2\text{O}$  ( $m/e = 44$ ). Fig. 7 shows the products and reactant evolution and the carbon and oxygen balance during the  $^{15}\text{NO}$  pulses over the  $\text{C}_3\text{H}_6$  reduced Pt/CZ at

**Table 1**  
Summary of TPR ( $\text{H}_2$ ),  $\text{H}_2$  consumption unit: mol  $\text{H}_2$ /mol Ce.

	Low temperature peak		High temperature peak		Total $\text{H}_2$ consumption
	T/°C	$\text{H}_2$ consumption	T/°C	$\text{H}_2$ consumption	
CZ	430	–	550	–	0.31
Pt/CZ	215	0.08	360	0.28	0.36
Rh/CZ	100	0.07	265	0.36	0.43

450 °C. As illustrated in Fig. 7, stage I and II were used to distinguish the full  $^{15}\text{NO}$  conversion time interval and the time intervals where NO started to breakthrough. Stage I was subdivided into stages Ia and Ib for the  $\text{CO}_2$  formation during stage I. During stage Ia (from pulse number 0 to 1000, Fig. 7A), full  $^{15}\text{NO}$  conversion was observed with  $^{15}\text{N}_2$  as the main product (negligible amount of CO formed). The evolution of  $\text{CO}_2$  was observed from pulse number 1000 (stage Ib, Fig. 7A).  $^{15}\text{NO}$  showed full conversion until pulse number 4000 (stage I, Fig. 7A), where  $^{15}\text{N}_2$  and  $\text{CO}_2$  were the only products. From pulse number 4000 onwards (stage II, Fig. 7A), a progressive decline to zero for the  $^{15}\text{NO}$  conversion was observed. The  $^{15}\text{N}_2$  and  $\text{CO}_2$  production followed the same trend as that of the NO conversion. Neither  $^{15}\text{N}_2\text{O}$  nor  $^{15}\text{NO}_2$  were formed and no traces of cyanide or cyanate containing species were detected. The oxygen, carbon and nitrogen balances were plotted as shown in Fig. 7B. During stage Ia (pulse number 0–1000, Fig. 7B), oxygen incorporation into catalyst was observed with a negligible amount of carbon consumption. The majority of the carbon conversion was found from

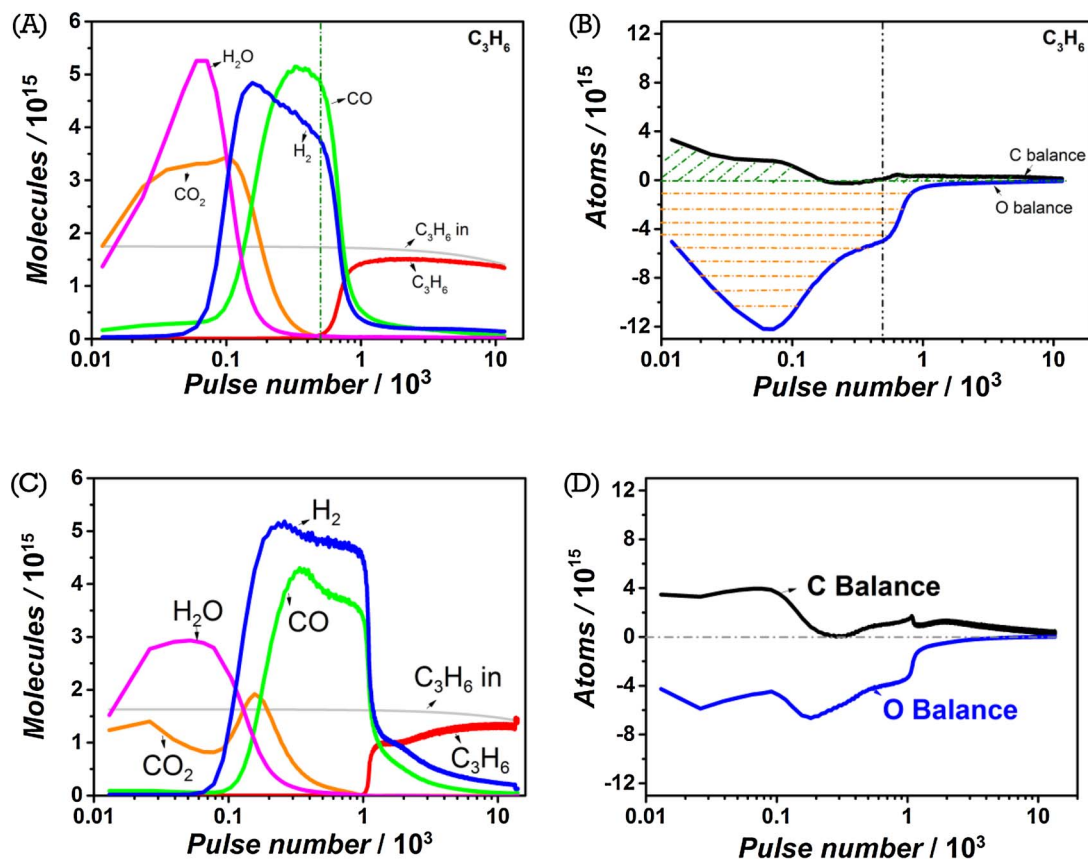


Fig. 5. C<sub>3</sub>H<sub>6</sub> pulses over a pre-oxidised 0.5 wt.% Pt/CZ and Rh/CZ (10 mg) at 450 °C, (A) and (C) product and reactant evolution, and (B) and (D) carbon and oxygen balance *versus* pulse number.

pulse number 1000 onwards (stage Ib), accompanied by an oxygen accumulation decline. Both oxygen accumulation and carbon consumption vanished after pulse number 6000. During stage I NO was fully converted, 80% of oxygen vacancies were refilled and 50% of the deposited carbon was oxidised. 17% of <sup>15</sup>N-species accumulated during the first 2000 <sup>15</sup>NO pulses, followed by the accumulated <sup>15</sup>N-species release as dinitrogen (N<sub>2</sub>) during pulse number between 2000 and 6000. The N-balance closed to 90%.

The result of <sup>15</sup>NO pulsing over a C<sub>3</sub>H<sub>6</sub> reduced Rh/CZ (Fig. 8) showed a similar trend as that over Pt/CZ. <sup>15</sup>NO started to breakthrough from pulse number 12,000 onwards, which was 3 times larger than that over Pt/CZ. However, a small amount of CO evolution was observed during stage Ia for the NO conversion on Rh/CZ. During stage I (the full NO conversion period), 80% of oxygen vacancies were refilled and 90% of carbon deposits were oxidised. Neither <sup>15</sup>N<sub>2</sub>O nor <sup>15</sup>NO<sub>2</sub> were formed and no traces of cyanide or cyanate containing species were detected during stages I and II. There was hardly any <sup>15</sup>N-species accumulation before pulse number 5000. After that <sup>15</sup>N species started to accumulate up to an N/O accumulation ratio of 1. Still a persistent <sup>15</sup>N<sub>2</sub> formation was observed after <sup>15</sup>NO started to breakthrough until

the carbon deposit had been consumed. The overall <sup>15</sup>N balance closed to 90%.

### 3.2.3. <sup>18</sup>O<sub>2</sub> pulses over C<sub>3</sub>H<sub>8</sub> reduced Rh/CZ

Fig. 9 shows the product evolution for the <sup>18</sup>O<sub>2</sub> multi-pulse experiment over C<sub>3</sub>H<sub>8</sub> reduced Rh/CZ at 450 °C. All introduced <sup>18</sup>O<sub>2</sub> was completely converted until a steep oxygen breakthrough profile was observed from pulse number 30,000 onwards. C<sup>16</sup>O evolved as the main product till pulse number 10,000, where C<sup>16</sup>O<sub>2</sub> started to evolve and gradually became the main product. After 13,000 pulses C<sup>18</sup>O<sup>16</sup>O was observed and a small amount of C<sup>18</sup>O<sub>2</sub> was detected after pulse number 15,000. After 28,000 pulses C<sup>16</sup>O, C<sup>16</sup>O<sub>2</sub>, C<sup>18</sup>O<sup>16</sup>O, C<sup>18</sup>O, and C<sup>18</sup>O<sub>2</sub> decreased to zero, where <sup>18</sup>O<sub>2</sub>, <sup>16</sup>O<sub>2</sub>, and <sup>18</sup>O<sup>16</sup>O started to breakthrough. With <sup>16</sup>O<sub>2</sub> as the main product after the oxygen breakthrough, a rapid exchange of oxygen with the CZ took place. The observed C<sup>18</sup>O (*m/e* = 30) during pulse number 13,000 to end of the pulse sequence was due to the fragmentation from C<sup>18</sup>O<sub>2</sub> and C<sup>18</sup>O<sup>16</sup>O. A small amount of C<sup>18</sup>O was also observed prior to pulse number 13,000, where the major product was C<sup>16</sup>O.

Table 2

Summary of oxygen extraction and carbon deposition using different reductants (O<sub>extracted</sub> and C<sub>deposited</sub> unit: 10<sup>17</sup> atoms / mg<sub>cat</sub>) at 450 °C.

	Pt/CZ			Rh/CZ		
	O <sub>extracted</sub>	O <sub>extracted</sub> removable from surface	C <sub>deposited</sub>	O <sub>extracted</sub>	O <sub>extracted</sub> removable from surface	C <sub>deposited</sub>
H <sub>2</sub>	2.1	0.8	Not applicable	2.2	0.9	Not applicable
CO	2.5	1	Not applicable	2.5	1	Not applicable
C <sub>3</sub> H <sub>6</sub>	6.3	2.5	2.8	8.2	3.2	8.0
C <sub>3</sub> H <sub>8</sub>	5.8	2.3	1.3	6.0	2.3	2.9

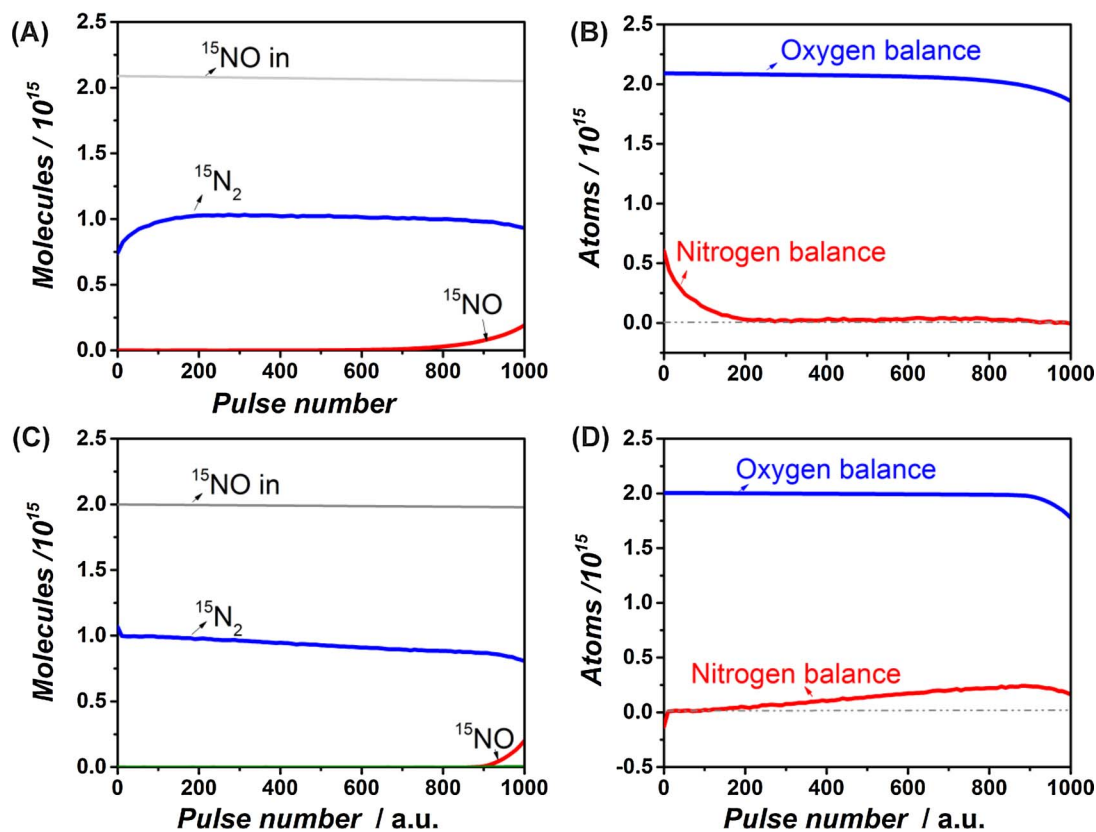


Fig. 6.  $^{15}\text{NO}$  multi-pulse experiment over  $\text{H}_2$  reduced (A, B) Pt/CZ (10 mg) and (C, D) Rh/CZ (10 mg) at 450 °C. Reactant and product profiles (A, C), and oxygen and nitrogen balances (B, D).

### 3.3. Pump-probe TAP experiments

In order to investigate the rate of  $\text{N}_2$  formation from NO over  $\text{H}_2$  reduced CZ and Rh/CZ, pump-probe TAP experiments were performed using alternating  $^{15}\text{NO}$  and  $^{14}\text{NO}$  pulses at 450 °C. The pulse size of  $^{15}\text{NO}$  and  $^{14}\text{NO}$  were both  $1.5 \cdot 10^{15}$  molecules/pulse. Fig. 10A and B shows the flux of  $^{14}\text{N}_2$ ,  $^{14}\text{N}^{15}\text{N}$ , and  $^{15}\text{N}_2$  during the  $^{15}\text{NO}$  and  $^{14}\text{NO}$  injections for the  $\text{H}_2$  pre-reduced CZ at 500 °C. The pulse of  $^{15}\text{NO}$  at  $t = 0$  s during first injection cycle led to the exclusive  $^{15}\text{N}_2$  formation. The total number of  $^{15}\text{N}_2$  molecules formed during the time interval of 5 s was calculated to be  $3.3 \cdot 10^{14}$  molecules. The maximum peak position of  $^{15}\text{N}_2$  was at  $t = 0.063$  s with peak height of  $1.3 \cdot 10^{15}$  molecules/s. The pulse of  $^{14}\text{NO}$  at  $t = 5$  s during the 1st injection cycle led to the formation of both  $^{14}\text{N}_2$  and  $^{14}\text{N}^{15}\text{N}$ . During the time from  $t = 5$  to 10 s, the number of  $^{14}\text{N}_2$  and  $^{14}\text{N}^{15}\text{N}$  was calculated to be  $3.7 \cdot 10^{14}$  and  $2 \cdot 10^{14}$  molecules, respectively.  $^{14}\text{N}^{15}\text{N}$  was also observed during the  $^{15}\text{NO}$  pulses after the first injection cycle. Moreover, an increase in the

intensity of  $^{14}\text{N}_2$ ,  $^{14}\text{N}^{15}\text{N}$ , and  $^{15}\text{N}_2$  were observed during the 40th injection as compared to 1st injection cycle. During the 70th injection cycle,  $8.8 \cdot 10^{14}$  molecules of  $^{15}\text{N}_2$  and  $8.1 \cdot 10^{14}$  molecules of  $^{14}\text{N}^{15}\text{N}$  were observed during  $^{15}\text{NO}$  injection, and  $8.3 \cdot 10^{14}$  molecules of  $^{14}\text{N}_2$  and  $8 \cdot 10^{14}$  molecules of  $^{14}\text{N}^{15}\text{N}$  were observed during  $^{14}\text{NO}$  injection.

Fig. 10C and D shows the flux of  $^{14}\text{N}_2$ ,  $^{14}\text{N}^{15}\text{N}$ , and  $^{15}\text{N}_2$  at the exit of the reactor over a  $\text{H}_2$  pre-reduced Rh/CZ. The pulse of  $^{15}\text{NO}$  at  $t = 0$  s in the first injection cycle led to the exclusive  $^{15}\text{N}_2$  formation with a peak position at  $t = 0.056$  s and peak height at  $5.5 \cdot 10^{15}$  molecules/s. The total number of  $^{15}\text{N}_2$  molecules formed during the time interval of 5 s was calculated to be  $7 \cdot 10^{14}$  molecules. The pulse of  $^{14}\text{NO}$  at  $t = 5$  s in the 1st injection cycle resulted in the formation of a major product of  $^{14}\text{N}_2$  with peak position at  $t = 5 + 0.056$  s and  $7 \cdot 10^{14}$   $^{14}\text{N}_2$  molecules formation during the time interval of 5 s. The peak height of  $^{14}\text{N}_2$  was identical to the  $^{15}\text{N}_2$  during the time period of 0–5 s. A small fraction of  $^{14}\text{N}^{15}\text{N}$  molecules, around 2–3% of  $^{14}\text{N}_2$ , were observed from  $t = 5$  to 10 s. After the first injection cycle, also a small fraction of  $^{14}\text{N}^{15}\text{N}$

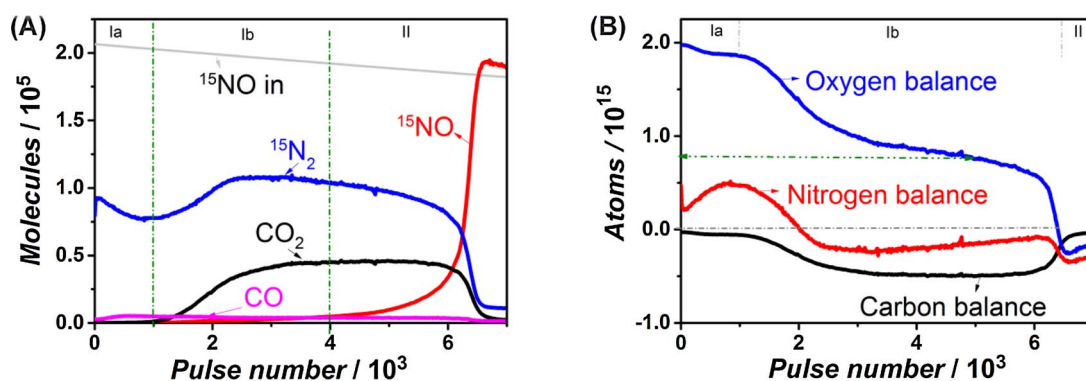


Fig. 7.  $^{15}\text{NO}$  multi-pulse experiment over  $\text{C}_3\text{H}_6$  reduced Pt/CZ at 450 °C, (A) products and reactant evolution and (B) carbon, oxygen and nitrogen balance versus pulse number.

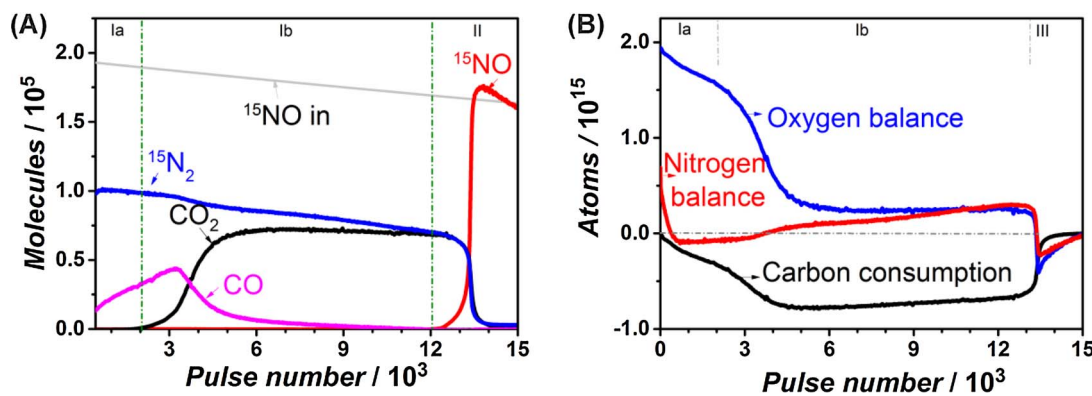


Fig. 8. <sup>15</sup>NO multi-pulse experiment over  $\text{C}_3\text{H}_6$  reduced Rh/CZ at  $450^\circ\text{C}$ , (A) products and reactant evolution, and (B) carbon, oxygen, and nitrogen balance versus pulse number.

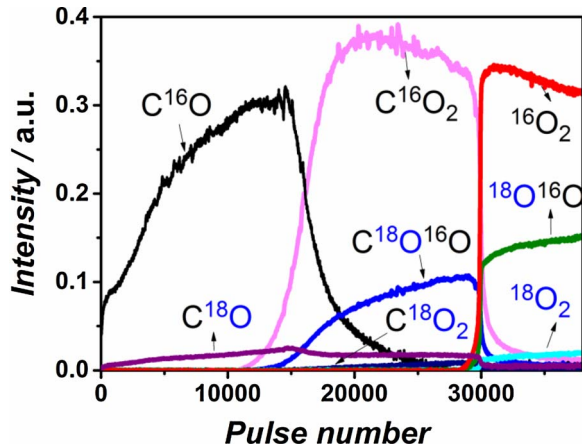


Fig. 9. Product and reactant evolution versus pulse number during  $^{18}\text{O}_2$  multi-pulse experiment over  $\text{C}_3\text{H}_6$  reduced Rh/CZ at  $450^\circ\text{C}$ .

(2–3% of  $^{15}\text{N}_2$ ) was observed during the  $^{15}\text{NO}$  pulses, as indicated for the 70th injection cycle (Fig. 10B).

#### 3.4. $\text{N}_2$ pulses over Rh/CZ and CZ

In order to explore the interaction of dinitrogen with CZ and Rh/CZ,  $^{14}\text{N}_2$  pulse experiments were performed over oxidised and reduced CZ and Rh/CZ. The Ar response was used as a standard reference response curve. Fig. 11A shows the  $\text{N}_2$  and Ar response shape over the CZ at  $500^\circ\text{C}$ . The  $\text{N}_2$  response showed peaks at  $t = 0.0672\text{ s}$  both over the oxidised and  $\text{H}_2$  reduced CZ. Moreover, the Ar peak located at the time of  $t = 0.0803\text{ s}$ . Both Ar and  $\text{N}_2$  showed the same response shape but with a shift of the peak position due to the difference in molar mass affecting the Knudsen diffusion coefficient [32]. Fig. 11B shows the  $\text{N}_2$  and Ar response shape over the Rh/CZ at  $450^\circ\text{C}$ . The  $\text{N}_2$  response showed a peak at  $t = 0.0674\text{ s}$  both over the oxidised and  $\text{H}_2$  reduced CZ, while the Ar peak position was at  $t = 0.0805\text{ s}$ .

#### 3.5. In-situ Raman study of $\text{C}_3\text{H}_6$ oxidation and NO reduction over Rh/CZ

Fig. S8 shows the in-situ Raman spectra during a continuous 1.25%  $\text{C}_3\text{H}_6/\text{He}$  flow at  $500^\circ\text{C}$  over Rh/CZ. The broad band from 100 to  $500\text{ cm}^{-1}$  was attributed to silica in the quartz tube. The sharp intensity centered at  $460\text{ cm}^{-1}$  was attributed to the symmetric stretch mode of the  $\text{Ce}-\text{O}_8$  crystal unit, characteristic for the fluorite ceria structure [33]. Its intensity started to drop after the first minute of  $\text{C}_3\text{H}_6$  exposure and disappeared two minutes after  $\text{C}_3\text{H}_6$  exposure, as shown in Fig. 12. Subsequently, two bands at  $1575$  and  $1350\text{ cm}^{-1}$  started to appear and grew during the prolonged  $\text{C}_3\text{H}_6$  exposure. The bands at  $1575$  and  $1350\text{ cm}^{-1}$  were assigned to the G band and D band of carbon [34]. The

G band was usually assigned to zone center phonons of  $E_{2g}$  symmetry of the perfect graphite structure and the D peak was assigned to a breathing mode of  $A_{1g}$  symmetry, which is forbidden in a perfect graphite structure and only became active in the presence of structural defects and disorders.

Fig. S9 shows in-situ Raman spectra for the NO reduction over  $\text{C}_3\text{H}_6$  reduced Rh/CZ at  $500^\circ\text{C}$ . As shown in the Fig. 13A, the sharp feature centered at  $460\text{ cm}^{-1}$  was initially hardly visible and its intensity slightly increased during the first 20 min upon 0.2% NO exposure. Moreover, it increased significantly after 60 min of NO flow exposure. Subsequently, the intensities at  $1575$  and  $1350\text{ cm}^{-1}$  strongly disappeared only after 90 min of NO exposure, as illustrated in Fig. 13B.

During the in-situ Raman experiment, the gas evolution downstream of the reactor was monitored with an MS and FT-IR spectrometer (Fig. 13C and D, respectively). Full NO conversion was observed till 60 min. Only  $m/e = 28$  was monitored, attributed from both  $\text{N}_2$  and CO. The FT-IR data showed that CO was only formed in the initial stage of NO exposure, declining after 20 min. After 20 min,  $m/e = 44$  appeared which was assigned to  $\text{CO}_2$ , since  $\text{N}_2\text{O}$  (detection limit  $< 1\text{ ppm}$ ) was not observed by FT-IR (Fig. 13D). Since the CO almost vanished around 30 min, the observed  $m/e = 28$  response from 20 to 60 min was mainly attributed to  $\text{N}_2$ .

## 4. Discussion

### 4.1. Reduction of noble metal loaded CZ

CZ is the essential catalyst ingredient in the Di-Air system, since it is capable of fuel (HCs) oxidation and NO reduction. The oxygen from the ceria lattice can react with hydrocarbon, CO, and  $\text{H}_2$ , thus creating oxygen vacancies and reducing  $\text{Ce}^{4+}$  to  $\text{Ce}^{3+}$ . Oxygen vacancies in reduced ceria are the catalytic sites for selectively converting NO into (di)nitrogen ( $\text{N}_2$ ), even in the presence of an excess  $\text{O}_2$  and  $\text{CO}_2$  [13]. However, the reduction of CZ with  $\text{C}_3\text{H}_6$  and  $\text{C}_3\text{H}_8$  required a temperature above  $500^\circ\text{C}$  and  $540^\circ\text{C}$ , respectively. Lowering the temperatures of CZ reduction by fuel is essential for an industrial application of this Di-Air  $\text{DeNO}_x$  system.

The TPR( $\text{H}_2$ ) (Fig. 4 and Table 1) showed that both noble metals lowered the reduction temperature of the CZ support as compared to the CZ support itself. This shift in reduction temperature might be associated with the  $\text{H}_2$  splitting on the noble metal and the existence of a strong metal-support interaction, increasing the reactivity of lattice oxygen [35]. The low temperature  $\text{H}_2$  reduction of both Pt/CZ and Rh/CZ led to  $\text{H}_2$  consumption of 0.08 and 0.07 mol  $\text{H}_2/\text{mol Ce}$ , which was larger than the amount needed for the reduction of metal oxide to metal. In addition, incorporation of hydrogen into ceria lattice in the form of hydroxyl group or hydride species were reported [36]. Therefore, the hydrogen consumption was a combination reduction of metal oxide to metal, a partial reduction of  $\text{CeO}_2$  into  $\text{Ce}_2\text{O}_3$ , and  $\text{H}_2$  storage.

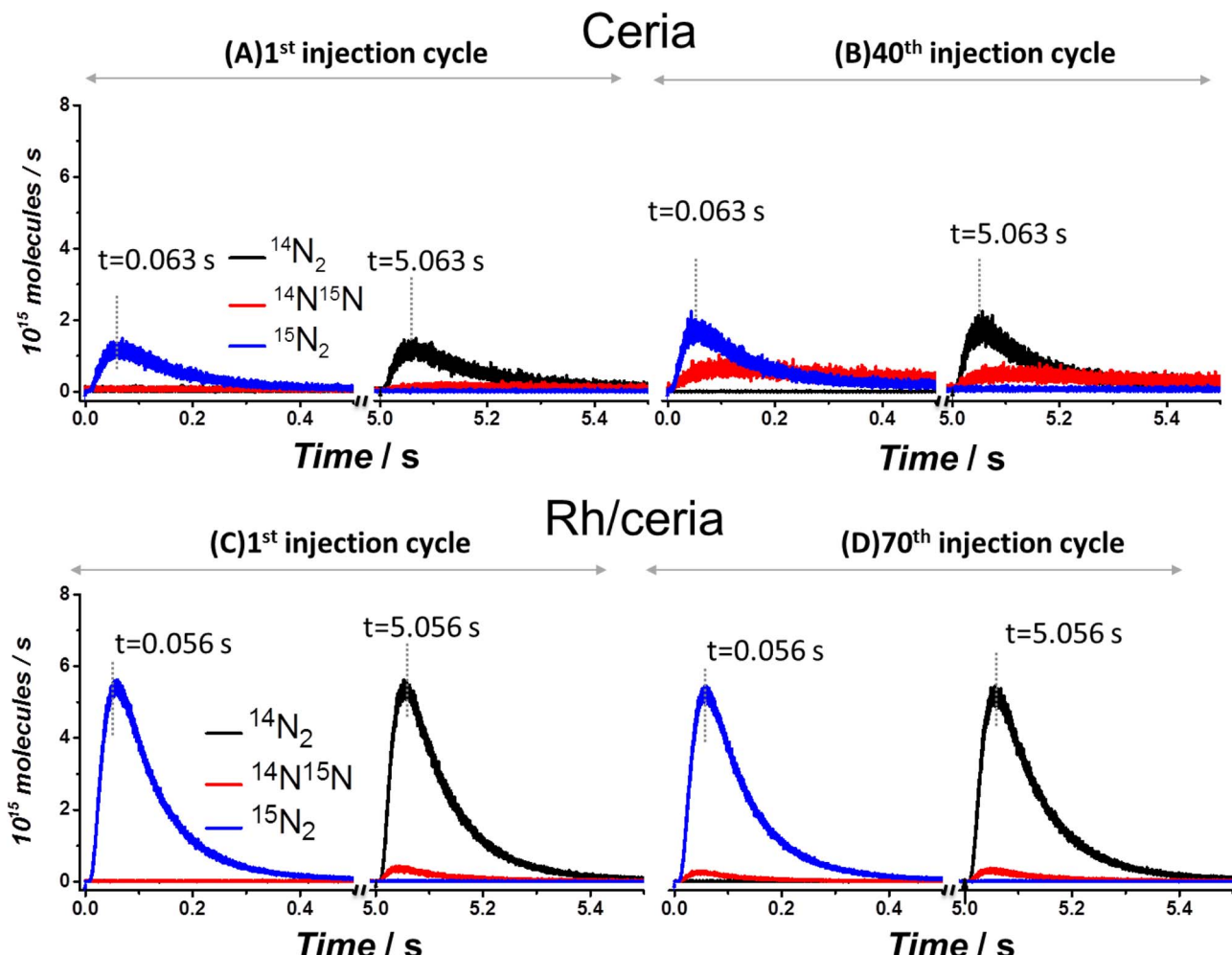


Fig. 10. The flux of  $^{14}\text{N}_2$ ,  $^{14}\text{N}^{15}\text{N}$ , and  $^{15}\text{N}_2$  during the alternate pulsing of  $^{15}\text{NO}$  and  $^{14}\text{NO}$  over a  $\text{H}_2$  pre-reduced (A and B) CZ at  $500\text{ }^\circ\text{C}$  and (C and D) Rh/CZ at  $450\text{ }^\circ\text{C}$ , measured at the exit of the reactor. The blue arrow indicated the pulse start of  $^{15}\text{NO}$  ( $t = 0$ ) and the black arrow for  $^{14}\text{NO}$  ( $t = 5\text{ s}$ ). Pulse size  $1.5 \cdot 10^{15}$  molecules. (It should be noted that the N-balance was calculated over the whole time interval of 5 s). (For interpretation of the references to colour in this figure legend, the reader is referred to the web version of this article).

The high intensity in the range of  $500$  and  $700\text{ cm}^{-1}$  on Rh/CZ and Pt/CZ from Raman spectroscopy (Fig. 2B) indicated a strong interaction between noble metal and CZ.

$\text{C}_3\text{H}_6$  and  $\text{C}_3\text{H}_8$  were fully converted over Pt/CZ for a pulse number of 100 and 50, respectively, to  $\text{CO}_2$  and  $\text{H}_2\text{O}$ , followed by a cracking reaction to  $\text{CO}$ ,  $\text{H}_2$ , and carbon deposition (Fig. 5A and B). The total amount of oxygen extracted from Pt/CZ by  $\text{C}_3\text{H}_6$  and  $\text{C}_3\text{H}_8$  was around

$6.3 \cdot 10^{17}$  and  $5.8 \cdot 10^{17}$  oxygen atoms/mg<sub>cat</sub> (Table 2), respectively. Additionally,  $2.8 \cdot 10^{17}$  and  $1.3 \cdot 10^{17}$  carbon atoms/mg<sub>cat</sub> were deposited after using  $\text{C}_3\text{H}_6$  and  $\text{C}_3\text{H}_8$  as reductant, respectively. So  $\text{C}_3\text{H}_6$  pulsing led to around 2 times higher carbon deposition than that for  $\text{C}_3\text{H}_8$  pulsing. Apparently, the reduction by  $\text{C}_3\text{H}_6$  or  $\text{C}_3\text{H}_8$  of an oxidised noble metal loaded CZ followed a similar process, but resulted in different carbon deposits. Dehydrogenation and cracking of  $\text{C}_3\text{H}_6$  was easier than

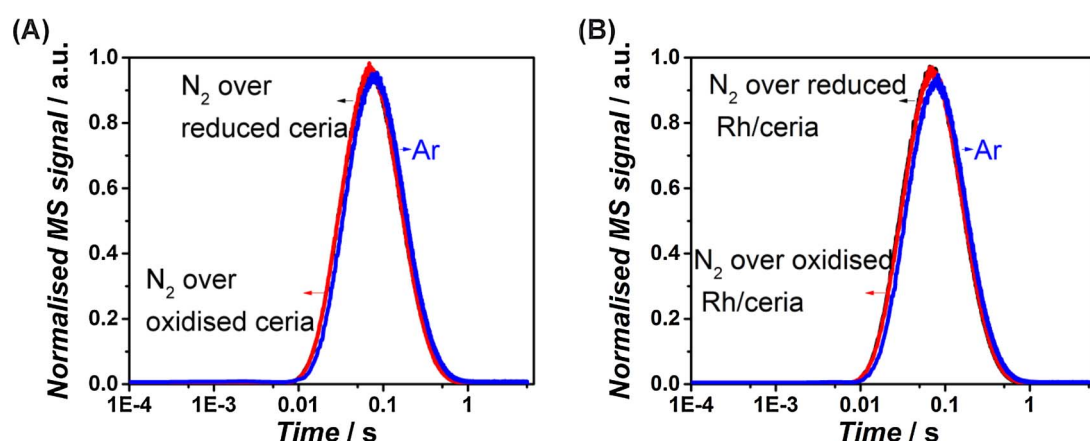


Fig. 11. Normalised MS responses of Ar (blue) and  $\text{N}_2$  pulses over oxidised (red) and reduced (black) CZ (A) and Rh/CZ (B). (For interpretation of the references to colour in this figure legend, the reader is referred to the web version of this article).

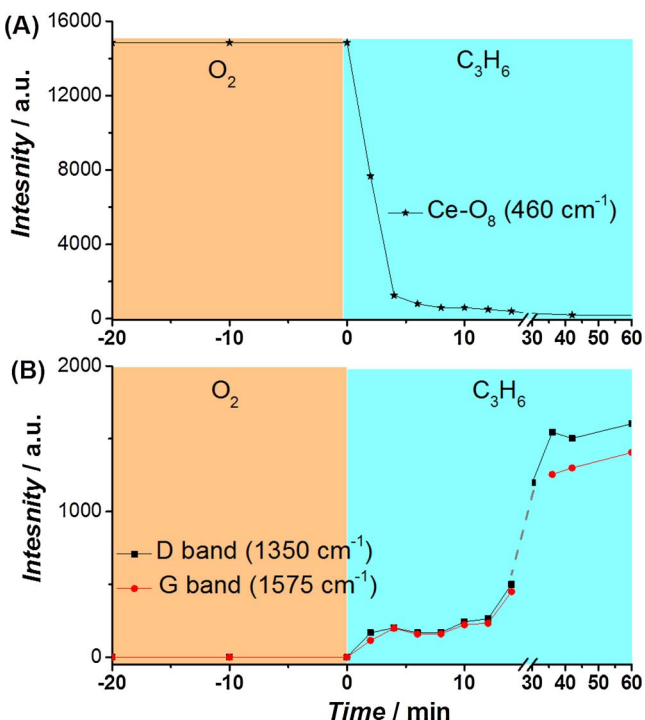


Fig. 12. Raman spectra of the band at (A)  $460\text{ cm}^{-1}$  and (B)  $1575$  and  $1350\text{ cm}^{-1}$  during  $\text{C}_3\text{H}_6$  exposure Rh/CZ at  $500^\circ\text{C}$ .

that of  $\text{C}_3\text{H}_8$  due to the strong electron-rich  $\pi$ -orbital interactions on Lewis acid sites [24], resulting in more carbonaceous deposits. Moreover, the results of oxygen balance, over either  $\text{C}_3\text{H}_6$  or  $\text{C}_3\text{H}_8$  pre-reduced Rh/CZ and Pt/CZ, indicated that the formation of  $\text{CO}_2$  and  $\text{H}_2\text{O}$  diminished at the point where the CZ surface was reduced. Therefore,  $\text{CO}_2$  and  $\text{H}_2\text{O}$  were formed over the oxidised CZ, which was in line with the results of CO and  $\text{H}_2$  pulsing experiments. Pulsing of  $\text{H}_2$  or CO led only to a surface reduction of CZ.

Pulsing  $\text{C}_3\text{H}_6$  and  $\text{C}_3\text{H}_8$  over Rh/CZ showed similar trends as for Pt/CZ. The total amounts of oxygen extracted from Rh/CZ by  $\text{C}_3\text{H}_6$  and  $\text{C}_3\text{H}_8$  were similar to that for Pt/CZ. However, the amount of deposited carbon over Rh/CZ was around 3 times larger than that on Pt/CZ when using  $\text{C}_3\text{H}_6$  as a reductant. Furthermore, the in-situ Raman experiment of passing 1.25%  $\text{C}_3\text{H}_6$ /He gas stream over Rh/CZ at  $500^\circ\text{C}$  (Fig. 13) showed that the reduction of the CZ support occurred firstly, followed by the subsequent deposition of carbon, in line with the results from TAP.

The CZ support was not reactive for  $\text{C}_3\text{H}_8$  and only slightly active for  $\text{C}_3\text{H}_6$  at  $450^\circ\text{C}$ . The addition of noble metals to the CZ support significantly enhanced the reactivities to  $\text{C}_3\text{H}_6$  and  $\text{C}_3\text{H}_8$ , i.e., the degree of CZ support reduction and the amounts of carbon deposition (Table 2). This agreed with the finding that noble metals were able to promote the oxygen mobility, surface migration, and reactivity, especially at the interface of noble metals and support [19].

#### 4.2. NO reduction

##### 4.2.1. Selectivity to $\text{N}_2$

$\text{NO}_2$  and  $\text{N}_2\text{O}$  are common side products in the NO reduction technologies especially when using noble metal as an active ingredient in the catalyst composition [37–40]. Therefore, the study on NO reaction processes over noble metal/CZ is essential.

$^{15}\text{N}_2$  was the exclusive product of  $^{15}\text{NO}$  reduction over the  $\text{H}_2$  reduced Pt/CZ and Rh/CZ (Fig. 6). After around 70–80% of oxygen vacancies was refilled by oxygen from  $^{15}\text{NO}$ ,  $^{15}\text{NO}$  started to breakthrough, while no  $\text{N}_2\text{O}$  and  $\text{NO}_2$  was formed. This was also observed for the bare CZ support [13]. The presence of Pt or Rh did not affect the NO reaction selectivity, i.e., NO was selectively reduced into  $\text{N}_2$ .

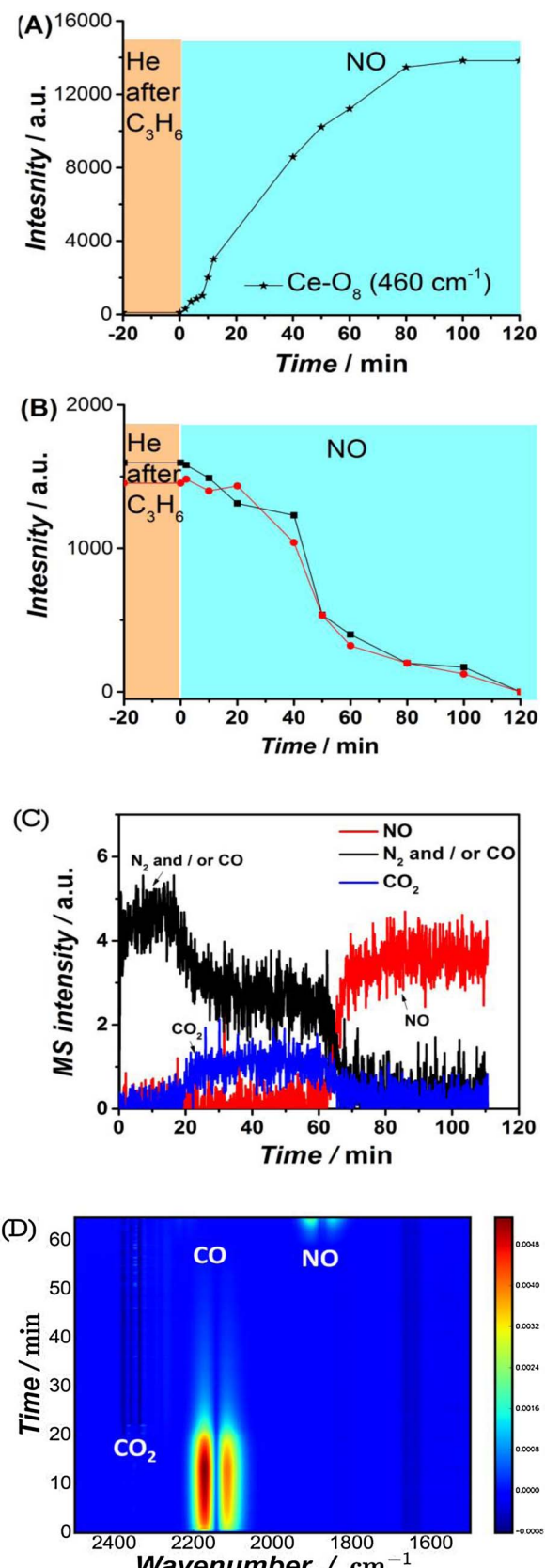


Fig. 13. Exposure of a  $\text{C}_3\text{H}_6$  reduced Rh/CZ to 0.2% NO at  $500^\circ\text{C}$ . Operando Raman spectra of the band at (A)  $460\text{ cm}^{-1}$  and (B)  $1575$  and  $1350\text{ cm}^{-1}$ , (C) MS analysis and (D) in-situ FT-IR analysis.

Moreover, when NO reduction was carried out over hydrocarbon reduced Pt/CZ then in the initial stage of  $^{15}\text{NO}$  pulsing no oxygenate gas products were observed at 450 °C (Fig. 7 for Pt/CZ). The absence of CO and  $\text{CO}_2$  indicated that the carbonaceous residues, left on the surface after  $\text{C}_3\text{H}_6$  pre-reduction, did not directly participate in the reduction of  $^{15}\text{NO}$  into  $^{15}\text{N}_2$ . The formation  $^{15}\text{N}_2$  indicated that  $^{15}\text{N}$ -O was dissociated on either the reduced Pt or reduced CZ sites with O filling the oxygen vacancies and  $^{15}\text{N}$  species associated to form  $^{15}\text{N}_2$ . The absence of  $^{15}\text{N}_2\text{O}$  indicated that  $^{15}\text{NO}$  was selectively reduced into  $^{15}\text{N}_2$  on the reduced Pt/CZ over the whole range of oxidation states of the catalyst. The  $^{15}\text{NO}$  started to breakthrough when ~80% of the oxygen vacancies were refilled and 50% of deposited carbon was consumed (Fig. 7B). The direct reaction between  $^{15}\text{NO}$  and deposited carbon could be ruled out since there was no  $\text{CO}_2$  formation before pulse number 1000. Approximately, the ratio between  $\text{N}_2$  and  $\text{CO}_2$  was around 2 during pulse number from 1000 to 4000, clearly demonstrated that for the formation of one  $\text{CO}_2$  two NO were reduced into one  $\text{N}_2$ . Therefore, the deposited carbon acted as a reductant buffer. Lattice oxygen of CZ was used for the oxidation of deposited carbon to CO and  $\text{CO}_2$ .  $^{15}\text{N}_2\text{O}$  and  $^{15}\text{NO}_2$  were never detectable (detection limit of 1 ppm). The direct reaction of  $^{15}\text{NO}$  molecules to  $^{15}\text{NO}_2$  over reduced Pt/CZ could be eliminated as well since carbon was an excellent reductant of  $^{15}\text{NO}_2$  to  $^{15}\text{NO}$  [41].

The overall performance of Rh/CZ (Fig. 8) was similar.  $^{15}\text{NO}$  started to break through much later than that over Pt/CZ. The longer duration of the full  $^{15}\text{NO}$  conversion was attributed to 3 times larger carbon deposition on Rh/CZ using  $\text{C}_3\text{H}_6$  as a reductant. This clearly demonstrated that deposited carbon acted as reductant buffer for NO reduction. NO reduction to  $\text{N}_2$  ended when there was no carbon left and the catalyst was (re-)oxidised. A small amount of CO was observed before the evolution of  $\text{CO}_2$  started during  $^{15}\text{NO}$  over the  $\text{C}_3\text{H}_6$  reduced Rh/CZ (phase II, Fig. 8A) in comparison with the case of Pt/CZ (Fig. 7A). However, the major initial  $^{15}\text{NO}$  reduction activity resulted in filling the oxygen vacancies, as evidenced by the oxygen balance and carbon balance (Fig. 8B).

An experiment of  $^{18}\text{O}_2$  pulses over the  $\text{C}_3\text{H}_8$  reduced Rh/CZ at 450 °C (Fig. 9) was performed to confirm that lattice oxygen was responsible for the oxidation of deposited carbon during stage Ib (Fig. 7 and 8). The results showed hardly any  $\text{C}^{18}\text{O}$  and  $\text{C}^{18}\text{O}_2$  formation prior to pulse number 13,000.  $\text{C}^{18}\text{O}^{16}\text{O}$  started to evolve after pulse number 13,000. The initial exclusive formation of unlabelled  $\text{C}^{16}\text{O}$  and  $\text{C}^{16}\text{O}_2$  indicated that gas-phase oxygen was not directly involved in the oxidation of the carbon deposits. Lattice oxygen was the main source for the oxidation of deposited carbon. After removal of the carbon deposit the  $^{18}\text{O}_2$  exchanged rapidly with the Rh/CZ resulting in predominantly  $^{16}\text{O}_2$ .

*Operando* Raman (at ambient pressure flow reactor) was applied to confirm further the results obtained from TAP (ultra-vacuum system,  $10^{-9}$ – $10^{-10}$  mbar) using Rh/CZ at 500 °C in flow reactor coupled with Raman probe, as shown in Fig. 13. The band at  $460\text{ cm}^{-1}$  (Fig. 13A), attributed to the symmetric stretch mode of  $\text{Ce}-\text{O}_8$  crystal unit in the oxidised catalyst [33], disappeared during the  $\text{C}_3\text{H}_6$  reduction pre-treatment (Fig. 12), while it reappeared and its intensity increased during the exposure to 0.2% NO/He. The changes of intensity at  $460\text{ cm}^{-1}$  indicated that the reduced CZ was re-oxidised during 0.2% NO/He flow. The intensities at  $1575$  and  $1350\text{ cm}^{-1}$ , assigned to *G* band and *D* band of carbon, remained almost constant during the first 20 min of 0.2% NO/He flows (Fig. 13B), and afterwards, these two bands completely vanished. The in-situ Raman results confirmed the TAP's finding: NO mainly re-oxidised the reduced CZ, and after a sufficient degree of re-oxidation the deposited carbon started to react with the oxygen from the CZ lattice. Upon NO exposure of the  $\text{C}_3\text{H}_6$  pre-treated catalysts (CZ and Rh/CZ) initially the reduced catalyst was oxidised and thereafter the carbon deposits were oxidised. This reduction-oxidation process could be completely repeated several times.

CO formation was observed during the first 20 min, followed by the

formation of  $\text{CO}_2$  till 60 min (Fig. 13C and D).  $\text{N}_2\text{O}$  and  $\text{NO}_2$  formations were not observed (detection limit < 1 ppm). Even  $\text{NO}_2$  and  $\text{N}_2\text{O}$  will be completely converted into  $\text{N}_2$  when the catalyst was reduced [42]. All results of this in-situ study (Fig. 13) pointed out that NO was still selectively reduced into  $\text{N}_2$  at these ambient pressure conditions. NO was dissociated on the active sites, being reduced CZ or reduced Rh sites, thereby filling the oxygen vacancies of CZ. In case of reaction on the noble metal the oxygen had to be transferred to the CZ since this was eventually completely re-oxidised.

The investigation of NO reduction under both ultra-high vacuum TAP system and at ambient pressure in a flow reactor pointed out that the presence of noble metal/CZ system can selectively reduce NO into  $\text{N}_2$  [13,17].

#### 4.2.2. The effect of noble metal on $\text{N}_2$ formation rate

During NO reduction over the  $\text{H}_2$  or  $\text{C}_3\text{H}_6$  pre-reduced un-promoted CZ, up to 25% and 40% of N-species accumulation was observed, respectively. The Pt promoted CZ showed only 17% of N-species accumulation and Rh promoted CZ showed hardly N-species accumulation before the oxidation of the carbon deposit. The N/O atomic accumulation ratio in that time interval suggested the same kind of NO chemisorption took place (Fig. 8B). The lower N-species accumulation on Rh- and Pt/CZ indicated that these metals accelerated the  $\text{N}_2$  release. In the formation of  $\text{N}_2$  the following steps can be distinguished: (1) NO adsorption, (2) NO dissociation, (3) N diffusion and association, and (4)  $\text{N}_2$  desorption. Pump-probe TAP experiments with alternating  $^{14}\text{NO}$  and  $^{15}\text{NO}$  pulse were performed to explore this  $\text{N}_2$  formation rate over CZ and Rh/CZ.

Over  $\text{H}_2$  reduced CZ only  $^{15}\text{N}_2$  formation was observed during the first  $^{15}\text{NO}$  pulse (Fig. 10A). However, the  $^{15}\text{N}_2$  response was much broader and lower in intensity than that for the  $\text{H}_2$  reduced Rh/CZ (Fig. 10C). The same holds for the  $^{14}\text{N}_2$  response during the  $^{14}\text{NO}$  injection. Both the  $^{15}\text{N}_2$  and  $^{14}\text{N}_2$  responses over the  $\text{H}_2$  reduced CZ indicated a slow process of dinitrogen formation upon the NO pulses. This process of  $\text{N}_2$  formation was that slow that some N-species were still sticking on the surface after the pulse detection time range (5 s). The observation of the mixed isotope  $^{14}\text{N}^{15}\text{N}$  during the subsequent  $^{14}\text{NO}$  injection suggested that stored  $^{15}\text{N}$ -species, during the  $^{15}\text{NO}$  injection, met  $^{14}\text{N}$ -species created after the following  $^{14}\text{NO}$  injection (Fig. 10B), and recombined to  $^{14}\text{N}^{15}\text{N}$ , and vice versa for the reversed sequence. The formation of  $^{14}\text{N}^{15}\text{N}$  further proved the accumulation of N ( $^{14}\text{N}$  and  $^{15}\text{N}$ ) species on the CZ surface that continued to the slow associate formation of dinitrogen. The mixed isotope response was much broader and its maximum appeared also later than the dinitrogen stemming directly from the pulsed NO isotope, both evidencing a slower recombination process for these "dwelling" nitrogen species.

Over the  $\text{H}_2$  reduced Rh/CZ a smaller fraction of  $^{14}\text{N}^{15}\text{N}$  was observed (Fig. 10C and D). This suggested that more N-species accumulated on the  $\text{H}_2$  reduced CZ than  $\text{H}_2$  reduced Rh/CZ. The N-balance in Fig. 6 also suggested that less N-species accumulated during the NO reduction to  $\text{N}_2$ . Almost all NO was converted and directly formed  $\text{N}_2$  during the MS detection time range (5 s) over the  $\text{H}_2$  reduced Rh/CZ before pulse number 200.

The  $\text{N}_2$  formation will include NO adsorption, NO dissociation, N diffusion and association, and  $\text{N}_2$  desorption. Regarding the NO adsorption, there was no  $^{15}\text{NO}$  or  $^{14}\text{NO}$  observed by the MS in the first  $^{15}\text{NO}$  or  $^{14}\text{NO}$  injection, i.e., all the  $^{15}\text{NO}$  or  $^{14}\text{NO}$  molecules were completely and irreversibly adsorbed over both  $\text{H}_2$  pre-reduced Rh/CZ and CZ. Therefore, the adsorption of  $^{15}\text{NO}$  or  $^{14}\text{NO}$  could not be the cause for the slow process of  $^{15}\text{N}_2$  or  $^{14}\text{N}_2$  formation over  $\text{H}_2$  reduced CZ. The possibility of  $^{15}\text{N}_2$  or  $^{14}\text{N}_2$  desorption as a limiting step could be ruled out by the experiments of pulsing  $\text{N}_2$  over CZ and Rh/CZ in fully reduced or oxidised state (Fig. 11), where  $\text{N}_2$  peak had at the same time position as the internal standard Ar response [43]. So once formed, the desorption of  $^{15}\text{N}_2$ ,  $^{14}\text{N}_2$  or  $^{14}\text{N}^{15}\text{N}$  was not a limiting step. Then, either the NO dissociation or N diffusion and recombination, or a combination

of these steps determined the slower  $^{15}\text{N}_2$  formation process over the reduced CZ.

The dissociation of NO on Rh single crystals was coverage dependent, which has been widely studied by temperature programmed desorption (TPD) [44]. NO dissociated completely at temperature between 0 and 70 °C, when the NO coverage was less than one fourth of the saturation coverage on Rh (1 1). Only 60% of the NO dissociated at saturation coverage, which was ascribed to site blocking. The accumulation of N and O atoms on the highly covered surface led to desorption of  $\text{N}_2$  at low temperature. Furthermore, Mullins and Overbury found that NO dissociated without  $\text{N}_2$  desorption at 175 °C over Rh/CeO<sub>2</sub>, which suggested that the desorption of  $\text{N}_2$  may be limited by the recombination of N-species on the surface [45]. The support had a strong influence on the NO dissociation. NO dissociation at 25 °C on highly dispersed Pt, Rh, and Pt + Rh supported on Al<sub>2</sub>O<sub>3</sub> and ceria showed that the ceria support limited the inhibition by the product oxygen, probably due to oxygen spill-over from the noble metal to reduced ceria [46], or an enhanced NO adsorption at the interface between ceria and Rh [47]. However, the changes in the ceria 4d photoemission showed that oxygen migration throughout the ceria only occurred above 25 °C [48]. 25 °C was too low for the substantial oxygen transport over the Rh substrate. The observed enhanced NO dissociation over a reduced ceria support at 25 °C could also not be attributed to oxygen spill-over from Rh to ceria support. Regarding N spill-over, soft X-ray photoelectron spectroscopy (SXPS) indicated that most N-species, resulting from NO dissociation remained on the Rh until they desorbed as  $\text{N}_2$ , rather than spilling over onto ceria. In addition, N spill-over did not occur at the temperature window from –80 to 80 °C [49]. Mullins and Overbury found the significant formation of  $\text{N}^{3-}$  over reduced ceria around 140 °C [50], but hardly over the reduced Rh/ceria [51]. The formation of  $\text{N}^{3-}$  was thermally activated, which did not form at temperature lower than 140 °C, although dissociation of NO and formation of  $\text{N}_2$  could occur below 140 °C. The recombination of  $\text{N}^{3-}$  into  $\text{N}_2$  occurred near 230 and 430 °C, which was higher than the  $\text{N}_2$  evolution via NO dissociation. The formation of  $\text{N}^{3-}$  required five Ce<sup>3+</sup> cations to dissociate one NO molecule. The slower  $^{15}\text{N}_2$  formation process over the reduced ceria at 500 °C in our study might be due to the formation of  $^{15}\text{N}^{3-}$ . Association of  $^{15}\text{N}^{3-}$  into  $^{15}\text{N}_2$  will be a slower process. By loading Rh over the ceria, the formation of  $^{15}\text{N}^{3-}$  species will be limited and  $^{15}\text{NO}^-$  species and  $^{15}\text{N}$ -species on Rh could be the dominant products, supported by SXPS spectra reported by Mullins and Overbury [50]. The faster  $^{15}\text{N}_2$  formation over reduced Rh/ceria than those over reduced ceria could be explained by these different NO dissociation products, i.e., NO- species or N-species over Rh/ceria and  $\text{N}^{3-}$  species over reduced ceria. The rate limiting step of NO reduction to  $\text{N}_2$  process over reduced ceria could be the step of  $\text{N}^{3-}$  species diffusion and its association into  $\text{N}_2$ .

In our study, the loading of Rh was 0.5 wt.% which corresponded to approximately 40 times more collisions of NO with CZ than those with Rh metal (calculation area ratio is shown in SI). NO absorbed over polycrystalline Rh with an initial sticking probability near unity [52]. Over the oxygen vacancies of reduced CZ surface, the sticking probability of NO adsorbing over the oxygen vacancies should be also really high, due to that no NO was observed both in TAP reactor [13] and flow reactor with space velocity up to 170.000 L/L/h [17] over an bare CZ catalyst. Therefore, it will be very unlikely that NO reduction into  $\text{N}_2$  process only occurred over the Rh metal. The enhanced  $\text{N}_2$  formation rate will be not due to the dissociation of NO over the Rh metal and the oxygen spill-over from Rh to metal. The faster  $\text{N}_2$  formation over Rh/CZ than that over CZ could be explained by that the noble metal largely limited the formation of  $\text{N}^{3-}$  species and accelerated the N species ( $\text{NO}^-$ , N) association process.

## 5. Conclusions

The addition of noble metals to CZ is essential for the selective NO

reduction. The noble metals Pt and Rh promote the CZ reduction by hydrocarbons C<sub>3</sub>H<sub>6</sub> and C<sub>3</sub>H<sub>8</sub>, at lower temperatures than that without these metals. Rh is a more active promoter in CZ Z reduction and carbon deposition than Pt. C<sub>3</sub>H<sub>6</sub> or C<sub>3</sub>H<sub>8</sub> leads to 2–2.5 times deeper reduction as compared to the CO and H<sub>2</sub>.

The reduction of NO over pre-reduced noble metal/CZ shows an extremely selective formation  $\text{N}_2$ , while neither  $\text{N}_2\text{O}$  nor  $\text{NO}_2$  formations are observed. More importantly, the presence of noble metal leads to a faster  $\text{N}_2$  formation rate than that over the CZ.

During the NO reduction the pre-reduced CZ support becomes gradually oxidised and after filling 70–80% of the oxygen vacancies the NO starts to appear in the product mixture. In the presence of carbon deposits the lattice oxygen of the CZ reacts with the carbon deposits keeping the CZ in a reduced state, extending the NO decomposition process as long as the carbon is present. Gas-phase oxygen does not directly react with the carbon. During the NO reduction process some unidentified N-species remain on the catalyst, the amount depending on the applied catalyst, but finally all nitrogen is released as  $\text{N}_2$ .

## Acknowledgement

The authors acknowledge the China Scholarship Council (CSC) for their financial support.

## Appendix A. Supplementary data

Supplementary material related to this article can be found, in the online version, at doi:<https://doi.org/10.1016/j.apcatb.2018.02.004>.

## References

- [1] <https://www.eea.europa.eu/publications/air-quality-in-europe-2015>, (Accessed 31 January 2018).
- [2] <http://www.who.int/mediacentre/news/releases/2014/air-pollution/en/>, (Accessed 31 January 2018).
- [3] <https://www.eea.europa.eu/data-and-maos/indicators/main-anthropogenic-air-pollutant-emissions-assessment-5>, (Accessed 31 January 2018).
- [4] D.C. Carslaw, S.D. Beavers, J.E. Tate, E.J. Westmoreland, M.L. Williams, Recent evidence concerning higher NO<sub>x</sub> emissions from passenger cars and light duty vehicles, *Atmos. Environ.* 45 (2011) 7053–7063.
- [5] [http://eropa.eu/rapid/press-release\\_MEMO-17-2821\\_en.htm](http://eropa.eu/rapid/press-release_MEMO-17-2821_en.htm), (Accessed 31 January 2018).
- [6] M. Koebel, M. Elsener, T. Marti, NO<sub>x</sub>-reduction in diesel exhaust gas with urea and selective catalytic reduction, *Combust. Sci. Technol.* 121 (1996) 85–102.
- [7] W.R. Miller, J.T. Klein, R. Mueller, W. Doelling, J. Zuerbig, The development of urea-SCR technology for US heavy duty trucks, *SAE Tech. Pap.* (2000) 2000-01-0190.
- [8] H. Hug, A. Mayer, A. Hartenstein, Off-highway exhaust gas after-treatment: combining urea-SCR, oxidation catalysis and traps, *SAE Tech. Pap.* (1993) 1993-03-01.
- [9] S. Matsumoto, Recent advances in automobile exhaust catalysts, *Catal. Today* 90 (2004) 183–190.
- [10] Y. Ikeda, K. Sobue, S. Tsuji, S. Matsumoto, Development of NO<sub>x</sub> storage-reduction three-way catalyst for D-4 engines, *SAE Tech. Pap.* (1999) 1999-01-1279.
- [11] M. Misono, T. Inui, New catalytic technologies in Japan, *Catal. Today* 51 (1999) 369–375.
- [12] Y. Bisaiji, K. Yoshida, M. Inoue, K. Umemoto, T. Fukuma, Development of Di-Air-a new diesel deNO<sub>x</sub> system by adsorbed intermediate reductants, *SAE Int. J. Fuels Lubr.* 5 (2012) 380–388.
- [13] Y. Wang, J. Posthuma de Boer, F. Kapteijn, M. Makkee, Next generation automotive DeNO<sub>x</sub> catalysts: ceria what else? *ChemCatChem* 8 (2016) 102–105.
- [14] H.C. Yao, Y.F.Y. Yao, Ceria in automotive exhaust catalysts: I. Oxygen storage, *J. Catal.* 86 (1984) 254–265.
- [15] Y. Wang, M. Makkee, Fundamental understanding of the Di-Air system (an alternative NO<sub>x</sub> abatement technology). I: the difference in reductant pre-treatment of ceria, *Appl. Catal. B Environ.* 223 (2018) 125–133, <http://dx.doi.org/10.1016/apcatb.2017.04.054>.
- [16] M. Inoue, Y. Bisaiji, K. Yoshida, N. Takagi, T. Fukuma, deNO<sub>x</sub> performance and reaction mechanism of the Di-Air system, *Top. Catal.* (2013) 1–4.
- [17] Y. Wang, R. Oord, D. van der Berg, B.M. Weckhuysen, M. Makkee, Oxygen vacancies in reduced Rh- and Pt-ceria for highly selective and reactive reduction of NO into  $\text{N}_2$  in excess of O<sub>2</sub>, *ChemCatChem* 9 (2017) 2935–2939.
- [18] Y. Wang, M. Makkee, The influence of CO<sub>2</sub> on NO reduction into  $\text{N}_2$  over reduced ceria-based catalysts, *Appl. Catal. B Environ.* 221 (2018) 196–205.
- [19] A. Holmgren, D. Duprez, B. Andersson, A model of oxygen transport in Pt/ceria catalysts from isotope exchange, *J. Catal.* 182 (1999) 441–448.
- [20] A. Bueno-López, K. Krishna, M. Makkee, Oxygen exchange mechanism between

isotopic CO<sub>2</sub> and Pt/CeO<sub>2</sub>, *Appl. Catal. A* 342 (2008) 144–149.

[21] L. Katta, P. Sudarsanam, G. Thrimurthulu, B.M. Reddy, Doped nanosized ceria solid solutions for low temperature soot oxidation: zirconium versus lanthanum promoters, *Appl. Catal. B: Environ.* 101 (2010) 101–108.

[22] V. Perrichon, A. Laachir, S. Abouarnadasse, O. Touret, G. Blanchard, Thermal stability of a high surface area ceria under reducing atmosphere, *Appl. Catal. A* 129 (1995) 69–82.

[23] Y. Wang, J.P. Boer, F. Kapteijn, M. Makkee, Fundamental understanding of the Di-Air system: the role of ceria in NO<sub>x</sub> abatement, *Top. Catal.* 59 (2016) 1–7.

[24] X. Wu, J. Fan, R. Ran, D. Weng, Effect of preparation methods on the structure and redox behavior of platinum–ceria–zirconia catalysts, *Chem. Eng. J.* 109 (2005) 133–139.

[25] S. Parres-Eslapez, I. Such-Basañez, M.J. Illán-Gómez, C. Salinas-Martínez de Lecea, A. Bueno-López, Study by isotopic gases and in situ spectroscopies (DRIFTS, XPS and Raman) of the N<sub>2</sub>O decomposition mechanism on Rh/CeO<sub>2</sub> and Rh/γ-Al<sub>2</sub>O<sub>3</sub> catalysts, *J. Catal.* 276 (2010) 390–401.

[26] A.A. Hakeem, J. Rajendran, F. Kapteijn, M. Makkee, Effect of rhodium on the water-gas shift performance of Fe<sub>2</sub>O<sub>3</sub>/ZrO<sub>2</sub> and CeO<sub>2</sub>/ZrO<sub>2</sub>: influence of rhodium precursor, *Catal. Today* 242 (Part A) (2015) 168–177.

[27] L.L. Murrell, S.J. Tauster, D.R. Anderson, Laser Raman characterization of surface phase precious metal oxides formed on CeO<sub>2</sub>, in: A. Crucq (Ed.), *Studies in Surface Science and Catalysis*, Elsevier, 1991, pp. 275–289.

[28] W. Lin, A.A. Herzing, C.J. Kiely, I.E. Wachs, Probing metal–support interactions under oxidizing and reducing conditions: in situ Raman and infrared spectroscopic and scanning transmission electron microscopic–x-ray energy-dispersive spectroscopic investigation of supported platinum catalysts, *J. Phys. Chem. C* 112 (2008) 5942–5951.

[29] A. Chen, Y. Zhou, N. Ta, Y. Li, W. Shen, Redox properties and catalytic performance of ceria–zirconia nanorods, *Catal. Sci. Technol.* 5 (2015) 4184–4192.

[30] N. Barrabés, K. Föttinger, A. Dafinov, F. Medina, G. Rupprechter, J. Llorca, J. Sueiras, Study of Pt-CeO<sub>2</sub> interaction and the effect in the selective hydrodechlorination of trichloroethylene, *Appl. Catal. B: Environ.* 87 (2009) 84–91.

[31] S. Penner, D. Wang, R. Podlucky, R. Schlägl, K. Hayek, Rh and Pt nanoparticles supported by CeO<sub>2</sub>: metal–support interaction upon high-temperature reduction observed by electron microscopy, *Phys. Chem. Chem. Phys.* 6 (2004) 5244–5249.

[32] G.S. Yablonsky, M. Olea, G.B. Marin, Temporal analysis of products: basic principles, applications, and theory, *J. Catal.* 216 (2003) 120–134.

[33] W. Weber, K. Hass, J. McBride, Raman study of CeO<sub>2</sub>: second-order scattering, lattice dynamics, and particle-size effects, *Phys. Rev. B* 48 (1993) 178.

[34] A. Ferrari, J. Meyer, V. Scardaci, C. Casiraghi, M. Lazzari, F. Mauri, S. Piscanec, D. Jiang, K. Novoselov, S. Roth, Raman spectrum of graphene and graphene layers, *Phys. Rev. Lett.* 97 (2006) 187401.

[35] J. Fan, X. Wu, R. Ran, D. Weng, Influence of the oxidative/reductive treatments on the activity of Pt/Ce0.67Zr<sub>0.33</sub>O<sub>2</sub> catalyst, *Appl. Surf. Sci.* 245 (2005) 162–171.

[36] J. Fierro, J. Soria, J. Sanz, J. Rojo, Induced changes in ceria by thermal treatments under vacuum or hydrogen, *J. Solid State Chem.* 66 (1987) 154–162.

[37] I. Atribak, B. Azambre, A.B. López, A. García-García, Effect of NO<sub>x</sub> adsorption/desorption over ceria–zirconia catalysts on the catalytic combustion of model soot, *Appl. Catal. B Environ.* 92 (2009) 126–137.

[38] Z. Wu, R. Jin, Y. Liu, H. Wang, Ceria modified MnO<sub>x</sub>/TiO<sub>2</sub> as a superior catalyst for NO reduction with NH<sub>3</sub> at low-temperature, *Catal. Commun.* 9 (2008) 2217–2220.

[39] G.R. Rao, P. Fornasiero, R. Di Monte, J. Kašpar, G. Vlaic, G. Balducci, S. Meriani, G. Gubitoso, A. Cremona, M. Graziani, Reduction of NO over partially reduced metal-loaded CeO<sub>2</sub>–ZrO<sub>2</sub> solid solutions, *J. Catal.* 162 (1996) 1–9.

[40] K. Krishna, A. Bueno-López, M. Makkee, J.A. Moulijn, Potential rare-earth modified CeO<sub>2</sub> catalysts for soot oxidation part II: characterisation and catalytic activity with NO + O<sub>2</sub>, *Appl. Catal. B Environ.* 75 (2007) 201–209.

[41] G. Mul, W. Zhu, F. Kapteijn, J.A. Moulijn, The effect of NO<sub>x</sub> and CO on the rate of transition metal oxide catalyzed carbon black oxidation: an exploratory study, *Appl. Catal. B Environ.* 17 (1998) 205–220.

[42] M. Nolan, S.C. Parker, G.W. Watson, Reduction of NO<sub>2</sub> on ceria surfaces, *J. Phys. Chem. B* 110 (2006) 2256–2262.

[43] J.T. Gleaves, G. Yablonsky, X. Zheng, R. Fushimi, P.L. Mills, Temporal analysis of products (TAP)—recent advances in technology for kinetic analysis of multi-component catalysts, *J. Mol. Catal. A Chem.* 315 (2010) 108–134.

[44] H. Borg, J.J. Reijser, R. Van Santen, J. Niemantsverdriet, The dissociation kinetics of NO on Rh (111) as studied by temperature programmed static secondary ion mass spectrometry and desorption, *J. Chem. Phys.* 101 (1994) 10052–10063.

[45] D. Mullins, S. Overbury, Coverage dependent dissociation of NO on Rh supported on cerium oxide thin films, *Surf. Sci.* 511 (2002) L293–L297.

[46] P. Lööf, B. Kasemo, S. Andersson, A. Prestad, Influence of ceria on the interaction of CO and NO with highly dispersed Pt and Rh, *J. Catal.* 130 (1991) 181–191.

[47] S.H. Oh, Effects of cerium addition on the CO–NO reaction kinetics over alumina-supported rhodium catalysts, *J. Catal.* 124 (1990) 477–487.

[48] D. Mullins, S. Overbury, D. Huntley, Electron spectroscopy of single crystal and polycrystalline cerium oxide surfaces, *Surf. Sci.* 409 (1998) 307–319.

[49] S. Overbury, D. Mullins, L. Kundakovic, Enhancement of dissociation by metal–support interaction: reaction of NO on Rh supported by ceria films of controlled oxidation state, *Surf. Sci.* 470 (2001) 243–254.

[50] S. Overbury, D. Mullins, D. Huntley, L. Kundakovic, Chemisorption and reaction of NO and N<sub>2</sub>O on oxidized and reduced ceria surfaces studied by soft x-ray photoemission spectroscopy and desorption spectroscopy, *J. Catal.* 186 (1999) 296–309.

[51] D. Mullins, L. Kundakovic, S. Overbury, The interaction between NO and CO on Rh-loaded CeO<sub>x</sub> (111), *J. Catal.* 195 (2000) 169–179.

[52] C.T. Campbell, J. White, Chemisorption and reactions of nitric oxide on rhodium, *Appl. Surf. Sci.* 1 (1978) 347–359.